

Abstract

Self-Assembly of Photonic Materials Beyond Crystals of Spheres: Amorphous Close-Packed Spheres and Crystalline Dumbbells

Jason D. Forster

2012

Crystalline packings of dielectric spheres with diameters of 100 to 400 nm can produce materials with photonic band gaps and are called photonic crystals. The periodic structure of these materials gives rise to constructive interference of visible light and these crystals can be brilliantly colored. Similarly, periodic structures in bird feathers and insect scales are responsible for many of the most striking colors found in the natural world. The basic scattering mechanism behind these iridescent colors is relatively straight forward and well described by Bragg scattering. Not nearly as well understood are the non-iridescent colors found in many bird feathers that are the result of scattering from disordered nano-structures. In this dissertation I aim to expand our understanding of structural color in two ways. First, I describe the design, assembly and characterization of isotropic structurally colored films of colloidal spheres and compare them to the non-iridescent structural colors of bird feathers. Second, I describe a new type of photonic crystal composed of dumbbell-shaped colloidal particles that combines the features of field switchable structural color and birefringence.

Self-Assembly of Photonic Materials

Beyond Crystals of Spheres: Amorphous

Close-Packed Spheres and Crystalline

Dumbbells

A Dissertation
Presented to the Faculty of the Graduate School
of
Yale University
in Candidacy for the Degree of
Doctor of Philosophy

by
Jason D. Forster

Dissertation Director: Eric R. Dufresne

May 2012

Copyright © 2012 by Jason D. Forster

All rights reserved.

Contents

1	Introduction	1
2	Biomimetic Isotropic Structures	5
2.1	Photonic Crystals	5
2.2	Avian Inspiration	8
2.3	Self-Assembly of an Isotropic Structure of Spheres	15
2.4	Suppression of Multiple Scattering by Absorption	20
3	Dumbbell Crystals	28
3.1	Anisotropic Particles: Colloidal Molecules	28
3.2	Dumbbells Crystallize Only Under Strong Confinement	29
3.3	Electric-Field Assisted Crystallization	31
3.4	Structural Properties of Dumbbell Crystals	39
3.5	Photonic Properties of Dumbbell Crystals	45
4	Conclusions and Future Work	49
4.1	Isotropic Structural Color	49
4.2	Dumbbell Crystals	51
4.3	Beyond Photonics	54

A Polymer Colloid Synthesis	59
A.1 Polystyrene Sulfonate Spheres	60
A.2 Poly(styrene-co-TMSPA) Core-Shell Spheres	61
A.3 Dumbbells	65

List of Figures

2.4	<i>Angle-resolved optical reflection spectra from C. maynana.</i> From Ref. [2].	10
2.5	<i>SAXS pattern from a hexagonal crystal has hexagonal symmetry. Left panel:</i> SEM image of an air-in-silica crystalline structure produced via a colloidal template following the procedure described in Ref. [1]. <i>Right panel:</i> SAXS pattern from the structure in the left panel. The hexagonal symmetry of the spots is a result of the hexagonal symmetry of the structure. The radial positions of the spots correspond to the lattice spacings in the structure. The log of intensity is plotted to improve contrast. The entire width of the image represents 0.43 nm^{-1} .	11
2.6	<i>SAXS pattern from an isotropic structure is a ring of uniform intensity. Left panel:</i> TEM image of the color-producing structure in the feathers of C. maynana. The scale bar represents 500 nm. <i>Right panel:</i> SAXS pattern from the structure on the left. The scale bar represents 0.025 nm^{-1} . From Ref. [2].	11
2.7	<i>Azimuthal average of SAXS pattern combined with optical reflection spectrum.</i> From Ref. [2].	13

2.8 <i>Effect of disorder and order on optical properties.</i> <i>a)</i> Photograph of a film of 226 and 271 nm PS spheres spin-cast onto an 18 × 18 mm glass coverslip. <i>Inset:</i> Photograph of a dried sessile droplet. <i>b)</i> Side-view SEM image a similar film. The field of view is 8.8 μm wide. <i>c)</i> The top set of curves show the transmission spectra for the isotropic film pictured in (a).The bottom set of curves show the results of the same measurement performed with a crystalline sample, made by spin-casting 226 nm PS spheres. The data were taken with the sample normal to the optical path (solid line), at an angle of 30° (dashed red line), and at an angle of 80° (dotted blue line), represented schematically in the upper left hand corner. <i>Inset:</i> Side-view SEM image of a crystalline sample, the field of view is 5.3 μm wide.	16
2.9 <i>Structure of isotropic films.</i> <i>a)</i> SAXS pattern from an isotropic film, the field of view is 0.15 nm^{-1} and the gray values are logarithmic in intensity. <i>b)</i> The azimuthal average of the experimental (red dots) and numerical (blue dashed line) scattering pattern. The black line is optical reflectivity data taken at an angle of 10° (experiment geometry shown in Figure 2.12) converted to q-space using an effective refractive index of $n_e = 1.24$	20

2.10	<i>Optimizing color by adding absorption.</i> a) Photograph of five drop-cast films of 226 and 265 nm PS spheres containing carbon black. Sample numbers and [CB] in wt% appear above and below the samples, respectively. b) Normalized optical scattering spectra recorded at an angle of 20° (experiment geometry shown in Figure 2.12) for the five samples in (a). <i>Inset:</i> Non-normalized scattering spectra for the same samples. c) SEM image of the interior region of sample 3, the field of view is 7.8 μm wide, a piece of CB is indicated with an arrow. d) The width of the spectra for each sample in (a) at $I(\lambda)/I(\lambda_0) = 0.90$	22
2.11	<i>Carbon black extinction length is inversely proportional to the concentration of [CB].</i>	24
2.12	<i>Color is the result of single scattering.</i> Normalized reflectance spectra taken over a range of angles and converted to q-space for sample 2 in Figure 2.10 (black lines), and the azimuthal average of the SAXS pattern for a similar sample (red dots). The spectra have been vertically offset for clarity. <i>Inset:</i> Position of the peak as a function of angle. <i>Schematic:</i> the source and sample are fixed and the detector is rotated.	26

2.13 Comparison with feathers. <i>a</i>) Photograph of crown feathers from <i>L. coronata</i> , the field of view is 1 cm. <i>b</i>) TEM image of air spheres in beta-keratin from <i>L. coronata</i> , the field of view is 5.5 μm . <i>c</i>) Azimuthal averages from SAXS measurements of <i>L. coronata</i> (dashed line) and a thick film with the same [CB] as sample 2 in Figure 2.10 (solid line). <i>Inset</i> : SAXS pattern from <i>L. coronata</i> , the field of view is 0.14 nm $^{-1}$ and the gray values are logarithmic in intensity. <i>d</i>) Comparison of optical scattering data taken at an angle of 20° (experiment geometry shown in Figure 2.12) from <i>L. coronata</i> and sample 2 from Figure 2.10. The line colors correspond to the apparent color of the feathers and the thick film.	27
3.1 <i>Dumbbells crystallize in confinement, but not in the bulk.</i> <i>a</i>), SEM image of dry dumbbells cast into thin films by vertical deposition. Dumbbells form ordered mono- and bi-layers [3]. <i>b</i>), SEM image of dumbbells cast into an amorphous thick film. The fields of view in (a) and (b) are 7.6 μm across.	30
3.2 <i>Sample chamber details.</i> <i>a</i>), Photograph of the sample chamber used to make dumbbell crystals. <i>b</i>), Schematic of the sample chamber. . .	32

3.3 <i>Aqueous suspensions of dumbbells display reversible crystallization in AC electric fields.</i> Aqueous suspension of dumbbells at volume fraction $\phi = 0.13$. <i>Top row</i> , Snap shots showing the onset of crystallization in an aqueous suspension of dumbbells in an AC electric field. The dark stripe across the bottom of the frame is a gold electrode. The sample is imaged through crossed polarizers. <i>Bottom row</i> , Snap shots showing the rapid loss of structural color and birefringence when the electric field is turned off. The whole process can be seen in Supplementary Movie 1 of Ref. [4]. The field of view in each image is 1.4 mm across.	33
3.4 <i>The timescales for the onset and disappearance of structural color and birefringence are very different.</i> Ratio of the intensity in the red channel to the total intensity from the video of <i>a</i>) crystal formation and <i>b</i>) crystal melting.	33

3.5	<i>Crystal structure of suspension dried in an AC electric field.</i> <i>a)</i> , SEM image of crystal formed by drying a suspension of dumbbells in the presence of an electric field. In this image, the electric field orientation is approximately vertical and the direction of flow due to drying is from right to left. The field of view is $27 \mu\text{m}$ across. <i>b)</i> , SEM image highlighting crystal structure. Two adjoining hexagons formed by the dumbbell lobes are highlighted by the yellow hexagons. The field of view is $3.6 \mu\text{m}$ across. <i>c)</i> , Model of the crystal structure suggested by SEM images. Two adjoining hexagons are highlighted and correspond to the highlighted facet in (b). <i>d)</i> , Packing fraction versus aspect ratio for crystalline structures (line) and random, jammed packings (circles) generated from numerical simulations described in the methods section. The packing fraction for the aspect ratio 1.58 dumbbells in a crystalline structure is $\phi = 0.7862$ (x).	34
3.6	<i>SEM images showing different cross-sectional views of a dumbbell crystal.</i> <i>a)</i> , The electric field direction relative to this image is approximately from bottom left to top right. <i>b)</i> , The electric field direction relative to this image is approximately into the page.	35
3.7	<i>SEM images showing details of a dumbbell crystal.</i> <i>a)</i> , The electric field direction relative to this image is approximately vertical. <i>b)</i> , The electric field direction relative to this image is approximately vertical.	36
3.8	<i>SEM image of a dumbbell crystal.</i> The electric field direction relative to this image is approximately horizontal.	37
3.9	<i>SEM image of a dumbbell crystal.</i> Low magnification SEM image of a dumbbell crystal. The Moire fringes in the image indicate that there is long-range order in the sample.	38

3.10 <i>The crystalline dumbbell structure described here is at least the densest local structure with respect to all possible linear strains of the cubic boundary.</i> To show this, we first create a mechanically stable crystalline packing by initializing the system with crystal positions and orientations and then apply the isotropic compression protocol to relax it. We obtain packing fractions $\phi_J \approx \phi_{xstal} + 10^{-8}$, which is consistent with the fact that the stopping criterion allows infinitesimal overlaps with $V/N\epsilon \approx 10^{-16}$. We then perturb the box shape using three orthogonal infinitesimal strains γ_{xy} , γ_{xz} , and γ_{yz} in both the positive and negative strain directions, and use the isotropic compression protocol at fixed strain to find the nearest mechanically stable packing with $\phi_J(\gamma)$. The packing fraction decreases, $\phi_{xstal} - \phi_J(\gamma) < 0$ for all aspect ratios and perturbations we studied.	40
3.11 Angle of dumbbell tilt that corresponds to the maximum packing fraction as a function of dumbbell aspect ratio, α	41
3.12 <i>Simulations demonstrate crystal formation depends strongly upon control of dumbbell orientation.</i> Probability of crystallization for a system of dumbbells as a function of aspect ratio. Systems with aligned dumbbells (squares) have significant probabilities of crystallization for most aspect ratios. Systems with unrestricted dumbbell orientations (circles) have near zero probabilities of crystallization for aspect ratios greater than 1.1. Each point is the result of 100 independent simulations. The two line types represent simulations performed with different quench rates, the dashed line has a quench rate that is 1000 times lower than the solid line.	44

3.13 Photonic band structure. <i>Left panel:</i> Photonic band structure, where D is the diameter of one dumbbell lobe, 267 nm for the dumbbells we use. <i>Right panel:</i> Illustrations corresponding to the crystal orientations for each wave vector.	46
3.14 Dumbbell crystals have a partial photonic band gap and are birefringent. <i>a),</i> Normal incidence reflection spectrum from a 70 μm x 70 μm area of a dumbbell crystal. The peak at 644 nm is close to the predicted photonic band gap position for the probed direction (band diagram in Figure 3.13). Images of <i>b)</i> the depth and <i>c)</i> phase of the modulation (in degrees) of transmitted light with the rotation of crossed polarizers measured at a wavelength of 650nm, which is inside the band gap. The electric field direction relative to this image is vertical. The field of view in both (b) and (c) is 600 μm across.	47
3.15 Images of <i>a)</i> the depth and <i>b)</i> phase of the modulation (in degrees) of transmitted light with the rotation of crossed polarizers measured at a wavelength of 534 nm, which is outside the band gap. The electric field direction relative to this image is vertical. The field of view in both (a) and (b) is 600 μm across.	47
4.1 Traditional inversion techniques cause cracking.	51
4.2 Simultaneous deposition of inorganic background and colloidal template prevents cracking.	52

4.3 <i>Amphiphilic dumbbells spread at an oil/water interface</i> <i>Top Row:</i> Still frames from a side-view movie of an aqueous droplet of dumbbells with an isotropic surface chemistry impacting an oil/water interface. <i>Middle Row:</i> Still frames from a side-view movie of an aqueous droplet of dumbbells with an amphiphilic surface chemistry impacting an oil/water interface. <i>Bottom Row:</i> Still frames from a top-view movie of an aqueous droplet of dumbbells with an amphiphilic surface chemistry impacting an oil/water interface. Frames in each row are separated from each other by 42 ms. The first image in the bottom row is 11 s after the drop impacted the interface.	55	
4.4 <i>Amphiphilic dumbbells impart elasticity to an oil/water interface.</i> Digital photographs of a membrane formed by amphiphilic dumbbells at a hexadecane/water interface being probed with a wooden stirrer.	56	
4.5 <i>Rhombic dodecahedra formed by capillary induced compression of toluene-swollen polystyrene spheres.</i>	58	
A.1 <i>Schematic of the synthesis procedure used to make dumbbells.</i> From Ref. [3]		59
A.2 <i>Polystyrene sulfonate sphere synthesis.</i>	62	
A.3 <i>Poly(Styrene-co-TMSPA) core-shell sphere synthesis.</i>	64	
A.4 <i>Dumbbell synthesis.</i>	67	
A.5 <i>High-magnification SEM image of dumbbells.</i> High-magnification SEM image of the same dumbbells in Figure A.4b. Note that the two lobes have differing degrees of roughness. The smoother lobe is primarily polystyrene and the rougher lobe is poly(styrene-co-TMSPA).	68	

Acknowledgements

I cannot imagine that I would have been able to get to this point in my scientific career without the steady flow of encouragement, excitement and support I have received from my advisor, Eric Dufresne. Over the years he has helped me in more ways than I can hope to describe here. There is, however, one piece of advice he gave me early on in graduate school that I have found particularly helpful and comforting. I don't remember his exact phrasing, but the message was, "If you think you know what you're doing, you're doing it wrong." I found that a particularly elegant and concise description of the real purpose of a Ph.D., to discover information about our universe that is not already known. Reminding myself that it is OK, even good, to feel lost and confused (at least once in a while) has not only helped in the lab but has become something of a guiding principle in my life. For this and much more, thank you.

As a member of the Soft Matter Lab I have had the opportunity to work with and learn from some of the smartest, most clever, most fun, and downright nicest people I have had the chance to meet. Because I do not know with whom I would stop, I am going to thank everyone my time has overlapped with. In ways big and small, clear and not clear to me, Vincent Germain, Sara Hashmi, Aric Sanders, Katie Kirkwood, Jacqueline Martinez, Stephen Chapin, Eleanor Millman, Kristina Mois, Elise Novitski, Cecile Mejean, Jason Merrill, Marleen van der Veen, Sunil Sainis,

Jin-Gyu Park, Wilfried Engl, Holger Kress, Alla Shundrovsky, Ye Xu, Madeleine Udell, Elissa Dunn, Elizabeth Jerison, Guy German, Alexandra Beautyman, Henry Foote, Aaron Mertz, Ross Boltiyanski, and Raphael Sarfati have all made an impact on me. Thanks to all of you.

It would be misleading of me if I didn't explicitly acknowledge the influence of Dr. Jin-Gyu Park. His dedication and imagination in the lab along with his ability to generate new and interesting particles is astounding and inspiring. None of the work in my dissertation would have been possible without his willingness to do the impossible — to teach chemistry to a physicist. Thank you!

I am grateful to have had the chance to collaborate with many exciting research groups at Yale. The groups of Hui Cao, especially Heeso Noh and Seng Fatt Liew, of Corey O'Hern, especially Carl Schreck, and of Richard Prum, especially Vinod Saranathan have been invaluable to my research. Also, I am grateful for the guidance and scientific advice I have received from Professors Simon Mochrie and Chinedum Osuji.

I have had the good fortune to collaborate with a number of groups and scientists outside of Yale. Especially important are the relationships I have had with Dr. Lin Yang from the National Synchrotron Light Source at Brookhaven National Labs and with Professor Eric Furst and his student Manish Mittal from the University of Delaware.

The physics faculty and my classmates from the physics department at Illinois Wesleyan University deserve many thanks for providing a great environment for my undergraduate education. I am particularly appreciative of Professor Gabe Spalding for giving me so much exposure to working in a lab. It is because of my research experience at Illinois Wesleyan that I was sure graduate school was the best next step for me.

If it weren't for the love and support of my family throughout graduate school and the 21 years before I would not have made it through the experience. My uncle Fred has been a constant, positive influence in my life and has never been short of good advice. My brother Andrew has kept me on my toes for as long as I can remember and has always let me know how proud he is. Most especially I want to thank my parents, Carla and Peter, for simultaneously letting me steer the course of my life and giving me the guidance to not run aground.

Anybody who has been my friend in New Haven has also had the great fortune to be the friend of my fiancée, Beezer (known to a few as Elizabeth). I could not ask for a more loving and supportive partner in my life and I can't thank you enough. I hope I can be as strong an ally and advocate for you as you have been for me.

Chapter 1

Introduction

The interaction of light and matter has held the interest of humans for millennia. A desire to understand this relationship has motivated physicists to study the fundamental nature of light and matter, enabled engineers to design and build myriad useful materials and devices, and given artists the tools to create so many culturally important and aesthetically pleasing works of art. Relevant to this dissertation are the methods for producing a material that reflects, scatters or absorbs light in the visible portion of the electromagnetic radiation spectrum. Specifically, I aim to broaden our understanding of light interacting with materials possessing a fine physical structure with characteristic dimensions on the order of hundreds of nanometers.

The property of a material that determines its interaction with light is the electric permittivity function, ϵ , which in general depends on the frequency of light, $\epsilon(\omega)$. Scattering, reflection, and refraction take place whenever light encounters an interface defined by a sudden difference in $\epsilon(\omega)$. Absorption can occur if $\epsilon(\omega)$ has an imaginary component. The index of refraction, n , of a material is a useful quantity to describe its interaction with light and is related to ϵ in a simple way, $n(\omega) = \sqrt{\epsilon(\omega)}$. Most of the materials I will describe in this dissertation are dielectric and thus do not have

significant absorption at optical frequencies. Furthermore, I will largely ignore the frequency dependence of the index of refraction because for the materials used here the value only varies by a few percent across the visible spectrum.

The particular form of an interface between differing indices of refraction has a dramatic effect on its scattering properties. When the interface is smooth compared to the wavelength of light we use the words reflection and refraction to describe the scattering. Smooth interfaces are responsible for phenomena like the reflected image of a mountain from the water/air interface of an alpine lake and the focusing of a collimated beam of light to a spot by a plano-convex lens.

More complicated scattering takes place when a material contains multiple interfaces. If n varies in a regular way and with a period comparable to the wavelength of light, scattering can lead to constructive interference of certain wavelengths of light and give the material a color — a structural color. This type of variation can be periodic in one, two, or three dimensions. Examples of this type of structural color are found in insect scales and bird feathers [5, 6, 7, 8, 9], as well as in opal gemstones [10]. Man-made materials with this property are often called photonic crystals. The scattering from these structures produces colors that change when viewed or illuminated from different directions, a phenomenon known as iridescence.

If the index of refraction varies in a disorganized way with no translational order the scattering of light is less discriminate. When the spatial distribution of scatterers is completely disordered, the material will appear white because it scatters all wavelengths of light with roughly equal efficiency [11]. Dilute colloidal suspensions such as milk appear white for this reason. However, systems with no translational order can have a structural color if the individual scatterers have a strong wavelength dependence. For example, if the scatterers are much smaller than the wavelength of light, the intensity of scattered light is inversely proportional to the fourth power

of the wavelength, $I \propto \lambda^{-4}$ [11]. This so-called Rayleigh scattering takes place as sunlight interacts with fluctuations in the local density of the gasses in Earth's atmosphere and explains why the sky away from the sun appears blue and the sun itself appears yellow during the day and red at sunset.

There are some materials that appear structurally disordered and yet selectively scatter a narrow range of wavelengths. The feathers of many birds contain one of two types of disordered scattering structures [2]. Both types are composed of air and a dried protein matrix of β -keratin. One of these structures is a bi-continuous network of air channels and β -keratin channels. The other is an array of spherical air inclusions in a background of β -keratin. At first glance, these structures appear to be completely disordered, but Fourier Transform analysis of electron-microscopy images [12] or small-angle X-ray scattering (SAXS) experiments [13] reveal that they possess a characteristic length scale without long range translational order. A consequence of this structure is that the colors produced are not iridescent — they appear to be the same from all angles. The development of these structures and the scattering mechanisms by which they produce color has been the subject of recent study [12, 2, 14, 15, 13].

A major focus of this dissertation is the design, assembly, and characterization of films that mimic these characteristics. The material we will use to assemble these structures are polymer colloidal spheres. This choice is based a number of factors, including the following: methods for synthesizing monodisperse spherical polymer colloids are well-established and have been applied in academia and industry for decades, it is possible to precisely control the size of the particles across a broad range of length-scales, and their rapid assembly into densely packed structures is aided by thermal fluctuations.

While making spherical colloids in large quantities has been possible for years,

only recently have techniques for synthesizing sub-micron colloids with anisotropic shapes and interactions been developed [16, 17, 3, 18, 19]. The second major focus of this dissertation takes advantage of this new-found capability by using dumbbell-shaped particles to assemble a photonic crystal with optical properties that cannot be replicated by a crystal of spheres.

In Chapter 2, I discuss the concepts relevant to photonic crystals and contrast them with materials possessing an isotropic structural color. First, I describe naturally occurring isotropic structural colors found in bird feathers in detail. Then I then describe the design, assembly, and characterization of materials composed of spherical colloidal particles that produce an isotropic structural color.

In Chapter 3, I describe a new type of photonic crystal composed of dumbbell-shaped colloidal particles. The anisotropic shape of the dumbbells allows us to make a field switchable birefringent photonic crystal.

In Chapter 4, I summarize the results and implications of the work in this dissertation and discuss possible directions for future research. First, I propose methods for improving the optical performance and functionality of isotropic structural color materials by inverting the structure formed by the spheres and applying an electric field. Then I propose new experiments to determine the crystal structure of dumbbells in an electric field and the potential for using dumbbells as colloidal surfactants.

Chapter 2

Biomimetic Isotropic Structures

2.1 Photonic Crystals

A material with a periodically varying index of refraction with a period on the order of the wavelength of visible light is called a photonic crystal. The first proposals for designing three-dimensional materials with such a property were published in 1987 by Yablonovitch [20] and John [21], but the study of naturally-occurring lower dimensional periodic structures can be traced to an 1885 publication by G. G. Stokes [22]. The theory of photonic crystals is often explained by analogy to electric semiconductors. In a semiconductor, one solves the Schrödinger equation for electrons in the material and finds that there is a range of energies that cannot propagate. Similarly, in a photonic crystal, one solves Maxwell's equations given the spatial variations of index of refraction in the material and finds a range of frequencies that cannot propagate. If there is a frequency range that cannot propagate in any direction the material is said to have a full photonic band gap. If there is a frequency range that can propagate in some directions but not others the material has a partial photonic band gap [23].

If light of a frequency that is not allowed in a photonic crystal is incident upon the crystal in the appropriate orientation, conservation of energy requires that it be reflected. When this frequency is in the visible, the crystal can appear brilliantly colored. A naturally occurring example of this is found in opal gemstones. Opals are composed of a crystalline packing of monodisperse silica spheres which have a size and index of refraction that is amenable to scattering visible light [10]. While solving Maxwell's equations is the most fundamental method for determining which frequencies are not allowed, applying the conditions for Bragg diffraction is a simpler method that is effective for analyzing crystalline structures with easily identifiable lattice planes. Bragg diffraction has been used to characterize atomic-scale crystal lattices by analyzing the constructive interference patterns of scattered X-rays which have wavelengths on the order of angstroms. Constructive interference of visible light takes place when the material has lattice spacings on the order of hundreds of nanometers. For a crystalline material with effective index of refraction, n_e , and a lattice spacing, d , the Bragg condition for constructive interference is

$$\lambda = 2n_e d \cos\theta, \quad (2.1)$$

where θ is the angle of incidence relative to the normal of the lattice plane and λ is the wavelength of light in free space. An illustration of the first few layers of a crystal of spheres and the relevant parameters for Bragg scattering is shown in Figure 2.1a. Figure 2.1b shows an SEM image of a photonic crystal composed of 286 nm diameter polystyrene spheres embedded in silica. The change in reflected color with angle of this sample is clearly seen in the photographs in Figure 2.1c and d.

In addition to the mineral example of opals there is a wide variety of photonic crystals found in the animal kingdom. The colors of many butterfly and beetle scales

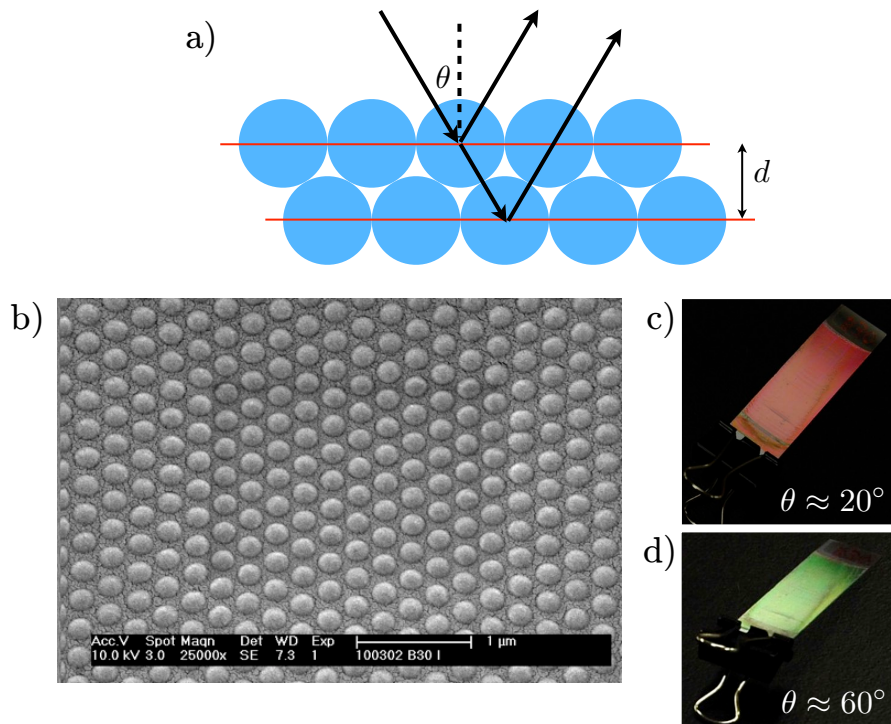


Figure 2.1: *Photonic crystal and Bragg scattering.* a) Schematic for Bragg scattering. b) SEM image of the top layer of a polystyrene-in-silica photonic crystal. This sample was produced following the procedure described in Ref. [1]. c) Color photograph of a specular reflection from the sample in (b) inclined approximately 20° relative to a white light source. d) Color photograph of a specular reflection from the sample in (b) inclined approximately 60° relative to a white light source.

and bird feathers are the result of scattering from crystalline structures produced by the organisms [6, 8, 5]. One striking feature of these kinds of structures is their iridescence — their color changes as they are observed from different directions or in different lighting conditions. The cause of this is readily apparent from Equation 2.1. For a given lattice spacing, the wavelength of light that constructively interferes is a function of θ and when illuminated by white light, the apparent color of the feather or scale changes as its orientation changes. Typically, the term *photonic crystal* is used to describe man-made materials, while *structural color* is used to describe biological examples because it emphasizes the fact that the color is the result of scattering, as opposed to absorption from a dye molecule. Examining the structures responsible for these iridescent colors reveals a variety of exotic structures that are frequently more complicated than the packings of spheres that make up an opal [6, 8, 5]. All of them, however, are clearly periodic and applying the concept of Bragg scattering allows one to accurately predict the resulting color from knowledge of the physical structure. Interestingly, there exist many examples of structural colors in bird feathers that are not iridescent [12, 13]. The microscopic structures in these feathers appear disordered and yet this structure is responsible for the color of the feathers. Without clearly identifiable lattice planes we cannot use Bragg scattering to explain this structural color phenomenon.

2.2 Avian Inspiration

Many species of birds have feathers that are brilliantly-colored without the use of pigments. Perhaps the most striking examples of structural color in nature are the iridescent colors created by scattering from periodic structures. Nature, however, also produces structural colors that have very little angle dependence. These colors

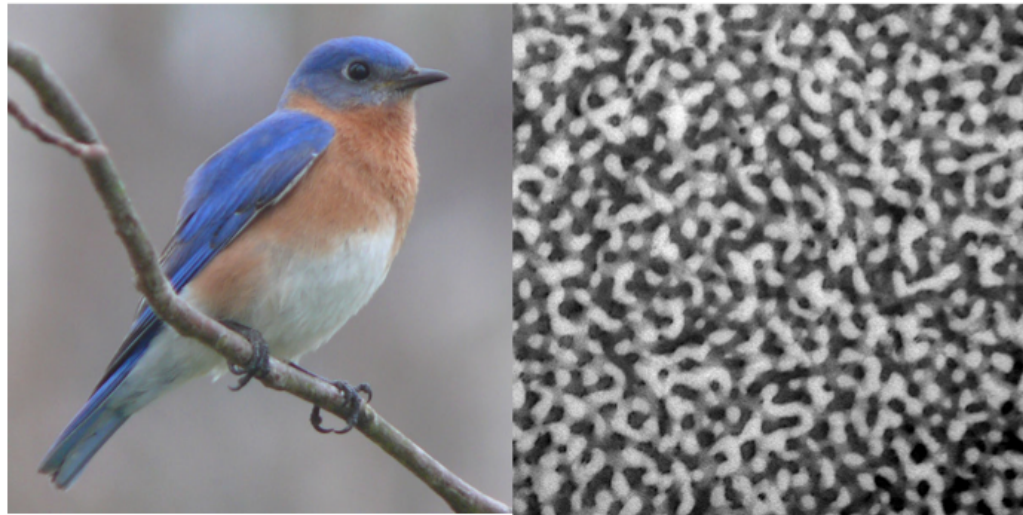


Figure 2.2: *The eastern blue bird displays isotropic structural color.* Left panel: Photograph of *Sialia sialis*. Right panel: TEM image of the channel-type structure responsible for the blue color of *S. sialis*. The light regions correspond to air channels and the dark regions correspond to β -keratin. The field of view is 4.5 μm across. Note: The reddish color of the chest feathers is not a structural color, it is the result of an absorbing dye. From Ref. [2].

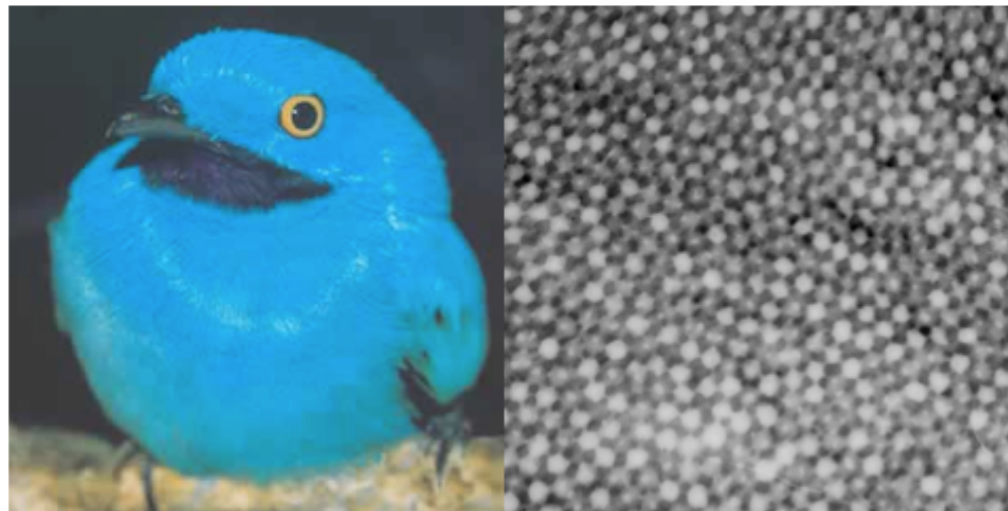


Figure 2.3: *The plum-throated cotinga displays isotropic structural color.* Left panel: Photograph of *Cotinga maynana*. Right panel: TEM image of the sphere-type structure responsible for the blue color of *C. maynana*. The light regions correspond to air pockets and the dark regions correspond to β -keratin. The field of view is 4.5 μm across. From Ref. [2].

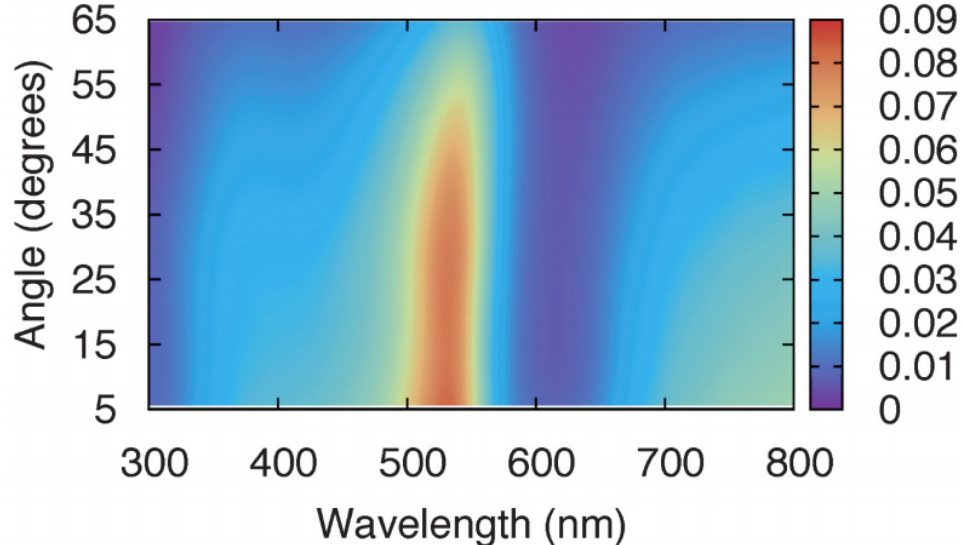


Figure 2.4: *Angle-resolved optical reflection spectra from *C. maynana*.* From Ref. [2].

are the result of scattering from isotropic structures [2, 14, 12]. Isotropic structural colors of bird feathers are produced by one of two classes of structures. One class is a bi-continuous network of air and β -keratin, which is called channel-type. An example of the channel-type structure is found in the eastern blue bird (*Sialia sialis*) and is shown in Figure 2.2. The other class is an array of spherical air pockets in a background of β -keratin, which we call sphere-type. The plum-throated cotinga (*Cotinga maynana*) has feathers with the sphere-type structure and is shown in Figure 2.3. Neither the channel- nor sphere-type structure has obvious lattice planes that we could use to predict their colors via Bragg scattering. Yet, as we can see in the reflection spectra recorded from *C. maynana* in Figure 2.4, the peak wavelength is not sensitive to the angle of observation. The question is then, how can these structures be responsible for scattering a narrow range of wavelengths? To answer this question, we need a method to quantify the 3D architecture of these structures.

The most fruitful technique we have employed in the characterization of these structures is small angle X-ray scattering (SAXS). SAXS involves imaging the scattering pattern produced as a collimated beam of X-rays is passed through the struc-

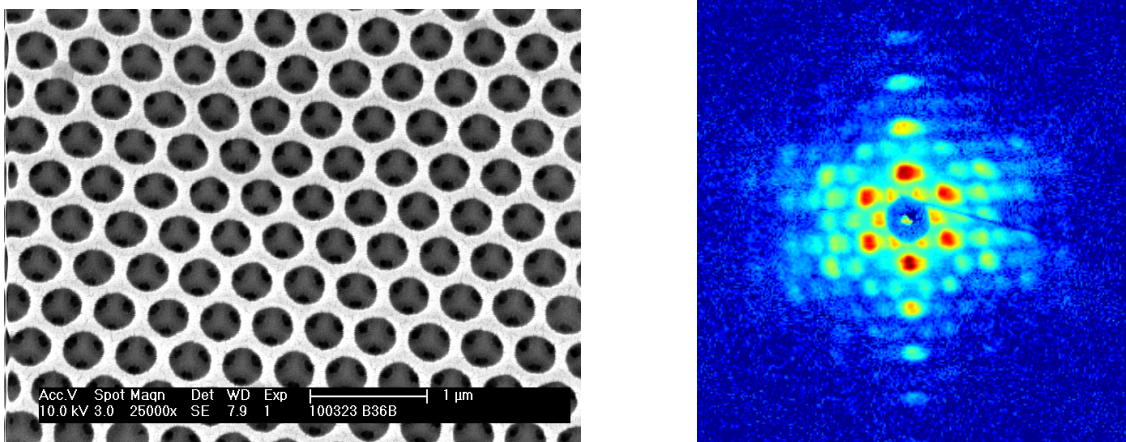


Figure 2.5: *SAXS pattern from a hexagonal crystal has hexagonal symmetry.* *Left panel:* SEM image of an air-in-silica crystalline structure produced via a colloidal template following the procedure described in Ref. [1]. *Right panel:* SAXS pattern from the structure in the left panel. The hexagonal symmetry of the spots is a result of the hexagonal symmetry of the structure. The radial positions of the spots correspond to the lattice spacings in the structure. The log of intensity is plotted to improve contrast. The entire width of the image represents 0.43 nm^{-1} .

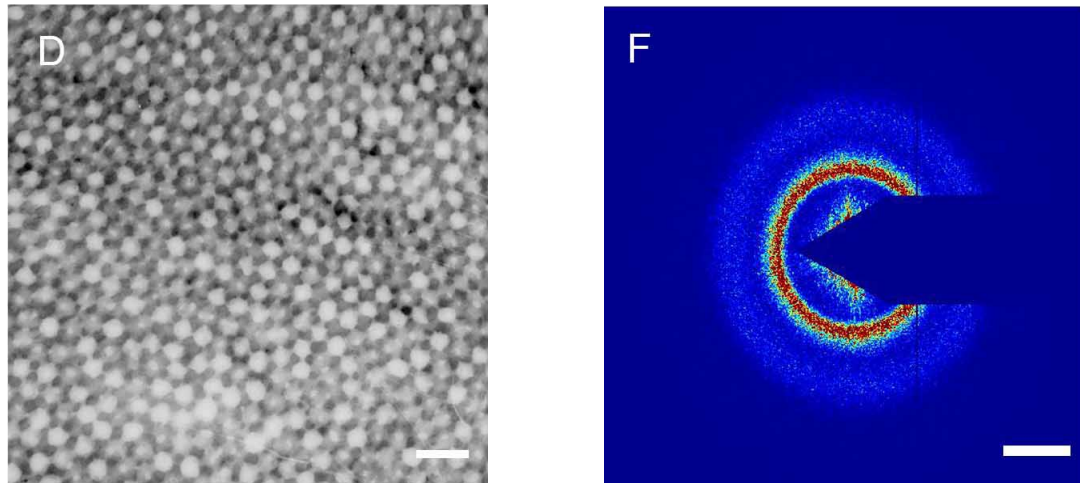


Figure 2.6: *SAXS pattern from an isotropic structure is a ring of uniform intensity.* *Left panel:* TEM image of the color-producing structure in the feathers of *C. maynana*. The scale bar represents 500 nm. *Right panel:* SAXS pattern from the structure on the left. The scale bar represents 0.025 nm^{-1} . From Ref. [2].

ture of interest. The scattering pattern contains a wealth of structural information: the radial position of a region of high intensity corresponds to a characteristic length scale in the scattering structure while the azimuthal distribution of intensity corresponds to symmetries in the structure. The scattering pattern produced by a crystalline material with grain sizes that are comparable to or larger than the spot size of the X-ray beam will consist of a set of bright spots, the radial positions of which correspond to the lattice spacing in the crystal and the symmetry of which correspond to the symmetry of the crystal structure. An example SAXS pattern from a photonic crystal is shown in Figure 2.5. In this case, a hexagonal crystal of air spheres in a silica background produces a scattering pattern with hexagonal symmetry. In contrast, materials that have a characteristic length scale but no long-range translational order will produce a scattering pattern in the form of a ring with uniform azimuthal intensity. The isotropic structure from *C. maynana* and the corresponding SAXS pattern are shown in Figure 2.6. The radius of the ring corresponds to the size of a dominant spatial correlation in the material and the absence of discrete points indicates a lack of long-range translational order. A crystalline material may produce a ring-like SAXS pattern if the grains are small compared to the beam size, but there are typically multiple well-defined rings, each corresponding to one of the various lattice spacings characteristic of the crystal structure. X-ray powder diffraction is a technique that takes advantage of this fact to identify the crystal structure of a material with small crystal grains [24]. The pattern in Figure 2.6, however, shows only two peaks and does not indicate the presence of any local crystalline order.

Combining structural information from SAXS with optical scattering measurements reveals that single scattering is primarily responsible for the color. In Figure 2.7, we directly compare an optical reflection spectrum (black line) to the az-

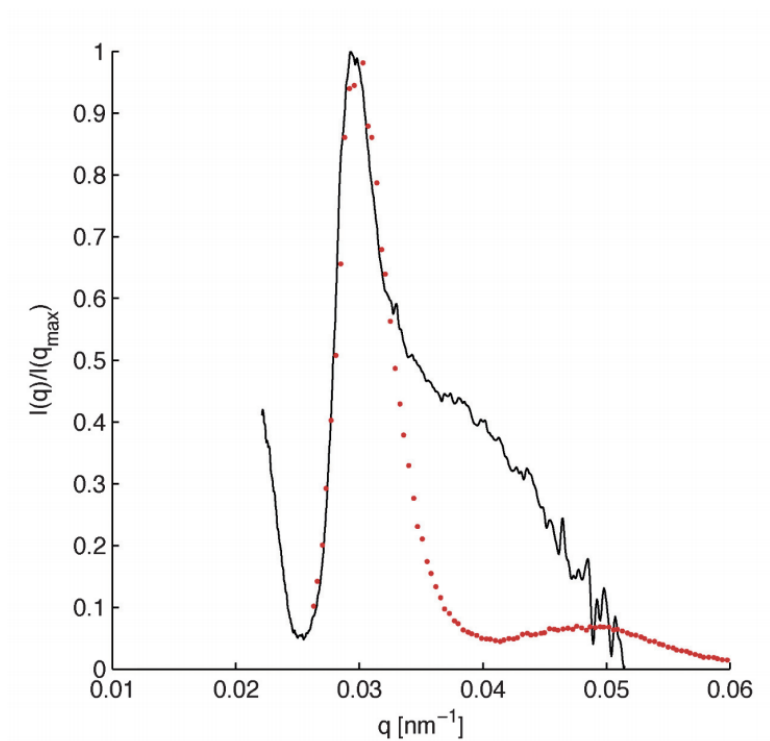


Figure 2.7: Azimuthal average of SAXS pattern combined with optical reflection spectrum. From Ref. [2].

imuthal average of the SAXS pattern in Figure 2.6 (red dots) by plotting the reflected intensity as a function of wavevector

$$q = \frac{4\pi n_e}{\lambda} \cos(\theta_m/2), \quad (2.2)$$

where n_e is the effective refractive index of the material; θ_m is the angle between illumination and detection, taking into account refraction at the film surface; and λ is the wavelength of light in vacuum. In general, the scattering intensity depends on wave vector, q , with the quantity $I(q)$ fully describing the spatial dependence of singly scattered light. Therefore, Eqn. 2.2 is a more general form of Bragg's Law (Eqn. 2.1), which only indicates the values of q where scattering is strongest. The index contrast between air and the protein matrix of the feathers for X-rays is very small, consequently, the scattering pattern we image in SAXS is the result of singly scattered photons. The fact that the first peaks from both measurements have nearly the same shape indicates that singly scattered photons in the optical range are responsible for the color [2]. The disagreement of the two curves at higher q can be attributed to multiple scattering events [25]. The first peaks of both measurements have nearly the same position when a value of 1.25 is used for n_e , indicating that air occupies 62% of the volume in this structure.

The goal of the next section is to design and assemble a material composed of spherical colloidal particles with the same structural and optical properties as these bird feathers.

2.3 Self-Assembly of an Isotropic Structure of Spheres

In recent years, periodic biological structures have provided inspiration for groups trying to make photonic materials [26, 7]. Much of this work has been motivated by producing a photonic band gap [20, 23, 27, 28, 9, 29]. However, Nature’s alternative design, based on isotropic structures is just starting to be explored [30, 31, 13]. Hallam *et al* have used biomimetic random structures to make ultra-thin mineral coatings that are brilliant white. Takeoka *et al* recently showed that a wide range of colors with very little angle dependence can be produced by microgel dispersions. In this section, we describe the self-assembly of biomimetic isotropic films which display structural color that is amenable to potential applications in coatings, cosmetics, and textiles. We find that isotropic structures with a characteristic length-scale comparable to the wavelength of visible light can produce structural color when wavelength-independent scattering is suppressed.

We make two types of films that are structurally-colored by exploiting the self-assembly of colloidal polymer nanoparticles. The first type of sample is a thin film on a glass coverslip produced by spin casting an aqueous suspension of spheres (Figure 2.8a). While monodisperse dispersions form anisotropic polycrystalline films, as shown in the inset of Figure 2.8c, a mixture of two sizes of spheres ensures an isotropic structure as shown in Figure 2.8b. The blue-green film in Figure 2.8 is made from a bidisperse suspension of polystyrene (PS) spheres with mean diameters of 226 and 271 nm and polydispersity 2% in equal volume fractions.

The synthesis of monodisperse PS spheres using surfactant-free emulsion polymerization is described in Appendix A.1 and in Ref. [32]. After synthesis, particle suspensions are washed by centrifugation and resuspension at least three times with DI water. After washing, the suspensions are adjusted to $\phi_{PS} = 0.3$. The sizes of

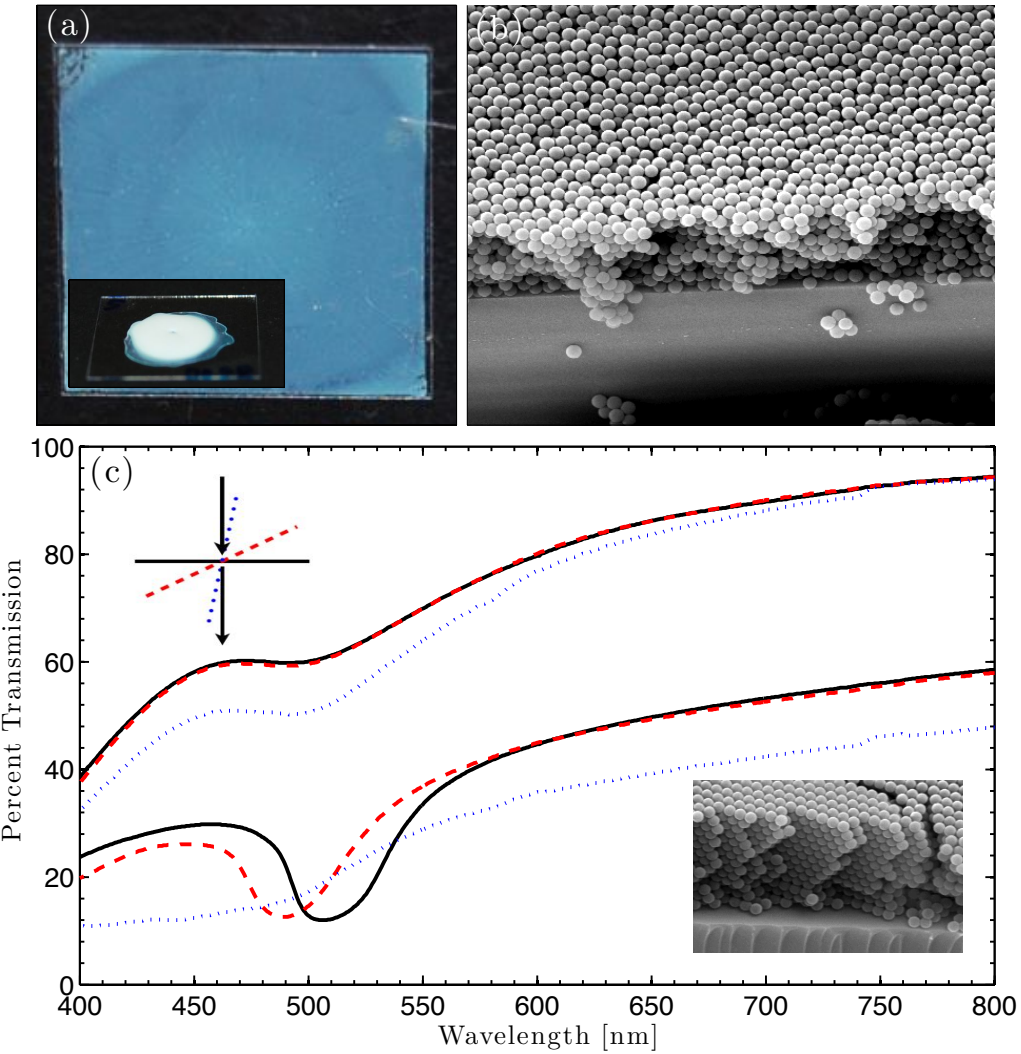


Figure 2.8: *Effect of disorder and order on optical properties.* a) Photograph of a film of 226 and 271 nm PS spheres spin-cast onto an 18×18 mm glass coverslip. Inset: Photograph of a dried sessile droplet. b) Side-view SEM image a similar film. The field of view is $8.8 \mu\text{m}$ wide. c) The top set of curves show the transmission spectra for the isotropic film pictured in (a).The bottom set of curves show the results of the same measurement performed with a crystalline sample, made by spin-casting 226 nm PS spheres. The data were taken with the sample normal to the optical path (solid line), at an angle of 30° (dashed red line), and at an angle of 80° (dotted blue line), represented schematically in the upper left hand corner. Inset: Side-view SEM image of a crystalline sample, the field of view is $5.3 \mu\text{m}$ wide.

particle are determined by scanning electron microscopy (SEM) image analysis using a Philips XL-30 ESEM with an accelerating voltage of 10 kV, after being coated with a thin layer of gold.

To prepare bidisperse suspensions, equal volumes of two monodisperse suspensions are mixed by pipetting approximately 20 times and vortexing for at least 30 seconds. Prior to spin casting for thin films or water evaporation for thick films, the suspensions are sonicated for at least 20 minutes to break up any aggregates. Thin films are spin cast onto glass coverslips cleaned with ethanol using a Headway Research, Inc. PWM32-PS-R790 spin coater. Typical spin speeds are between 500 and 5000 RPM, the spin speed and viscosity of the suspension determine the final thickness of the film [33].

The side-view SEM in Figure 2.8b is of a film comparable to the one in Figure 2.8a and shows that there is no long range order, it also reveals a representative thickness of $2.3 \pm 0.2 \mu\text{m}$.

The optical properties of isotropic and crystalline films are quite different, even for samples prepared with very similar particles. We compare the transmission spectra of isotropic and crystalline samples in Figure 2.8c. Transmission spectra are measured using a Hitachi U-2001 spectrophotometer. The isotropic film is the same one pictured in Figure 2.8a, the crystalline film is composed solely of the 226 nm spheres. Both samples show a dip near 500 nm at normal incidence. However, when the angle of incidence is changed, the spectral position of the dip for the crystalline sample shifts and eventually disappears. In contrast, the position of the dip for the isotropic sample does not move. This illustrates the trade-off in optical performance between crystalline and isotropic structures: while the crystalline film has more pronounced features at some angles, the isotropic film performs consistently over a wide range of angles.

To quantify the structure of the films, we perform small-angle X-ray scattering (SAXS) measurements on samples composed of spheres with mean diameters of 226 and 265 nm with 2% polydispersity, spin-cast on kapton tape. A typical scattering pattern is shown in Figure 2.9a. The pattern is dominated by a ring of uniform intensity, indicating that there is a well-defined length scale with no preferred direction — the structure is isotropic with short-range order. The azimuthal average of this pattern is shown in Figure 2.9b, along with the expected scattering intensity from simulations of jammed packings of bidisperse spheres with size and number ratios that match our experimental system. The position of the first peak in $I(q)$ occurs at $q_0 = 0.03 \text{ nm}^{-1}$ for both simulation and experiment. The full width at half maximum (FWHM) of the first peak, Δq , characterizes the range of spatial order $\xi = 2\pi/\Delta q = 870 \text{ nm}$. In powder crystallography, ξ describes the crystal domain size, here, ξ is only a few particle diameters.

SAXS measurements of biomimetic samples are carried out at beamline X9 at the NSLS, Brookhaven Naitonal Laboratory, using a Rayonix Mar 165 CCD detector. The X-ray energy is 7 keV (a wavelength of 1.771 Å) and the sample-to-detector distance is 5 m. The conversion from the detector image to reciprocal space is calibrated using the diffraction pattern from a standard silver behenate sample ($q_0 = 0.1076 \text{ \AA}^{-1}$). The first ring from silver behenate is out of the angular range covered by the detector at 7 keV, therefore the standard pattern was collected with the same scattering geometry but at an X-ray energy of 15.65 keV (0.792 Å). The finite beam size at the detector corresponds to FWHM q resolution of 0.00045 \AA^{-1} , which is $\sim 17\%$ of the width of the fringe produced by the spheres ($\pi/120 \text{ nm} \approx 0.0026 \text{ \AA}^{-1}$). Biomimetic samples for SAXS measurements are prepared on 0.0025"-thick Kapton Tape, purchased from McMaster-Carr (catalog no. 7648A33).

To simulate the structure of our samples, we create mechanically stable packings

of bidisperse frictionless spheres in cubic cells with periodic boundary conditions using a simulation protocol in which we successively compress/decompress soft particles and then apply conjugate gradient energy minimization until particles are just at contact (up to a prescribed energy threshold) [34]. The energy threshold, initial packing fraction ϕ_0 , and increment in ϕ are set to 10^{-8} , 0.2 and 10^{-4} , respectively. We select particle size and number ratios to match the experiments. From 50 independent initial configurations, we obtain an average packing fraction $\phi_J = 0.63$, which is relatively insensitive to the specific parameters of the packing-generation protocol. From the particle centers, we calculate the partial, $S_{ll}(q)$, $S_{ss}(q)$, and $S_{ls}(q)$, and total structure factor

$$S(q) = x_l S_{ll}(q) + x_s S_{ss}(q) + 2\sqrt{x_l x_s} S_{ls}(q), \quad (2.3)$$

where l, s signify large or small particles, x is the number fraction of the indicated particle, and q is the wavevector. The partial structure factors and the theoretical form factors for each sphere size are used to calculate the total scattering intensity

$$I(q) \propto x_l S_{ll}(q) F_l^2(q) + 2\sqrt{x_l x_s} S_{ls}(q) F_l(q) F_s(q) + x_s S_{ss}(q) F_s^2(q). \quad (2.4)$$

We directly compare optical reflectivity measurements to SAXS measurements in Figure 2.9b by plotting the reflected intensity as a function of wavevector using Eqn. 2.1. The peaks from both measurements match when $n_e = 1.24$. We apply the Maxwell-Garnett equation,

$$n_e = n_{air} \left(\frac{2n_{air}^2 + n_{PS}^2 + 2\phi(n_{PS}^2 - n_{air}^2)}{2n_{air}^2 + n_{PS}^2 - \phi(n_{PS}^2 - n_{air}^2)} \right)^{1/2} \quad (2.5)$$

to calculate the volume fraction of spheres, $\phi = 0.46 \pm 0.04$, where n_{PS} is the index of

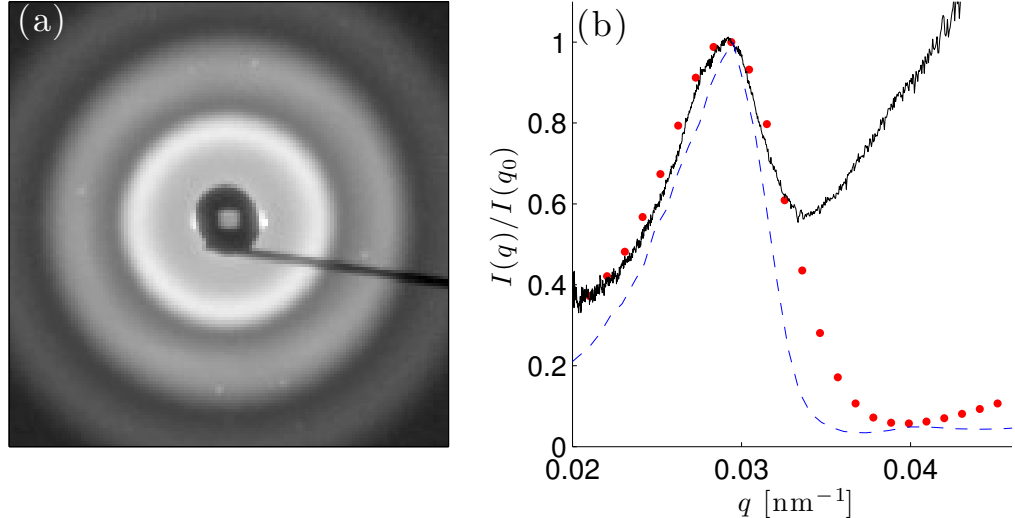


Figure 2.9: *Structure of isotropic films.* *a)* SAXS pattern from an isotropic film, the field of view is 0.15 nm^{-1} and the gray values are logarithmic in intensity. *b)* The azimuthal average of the experimental (red dots) and numerical (blue dashed line) scattering pattern. The black line is optical reflectivity data taken at an angle of 10° (experiment geometry shown in Figure 2.12) converted to q -space using an effective refractive index of $n_e = 1.24$.

refraction of the spheres, taken to be 1.58, and n_{air} is taken to be 1.00. The optical reflection and scattering spectra were performed with a custom-built setup in Hui Cao's laboratory described in detail in Noh *et al* [15].

2.4 Suppression of Multiple Scattering by Absorption

Isotropic films can produce structural color with little angle dependence, but the film thickness critically affects its color, as seen in the inset of Figure 2.8a. Here, we cast a thick film by drying a sessile droplet of the same suspension used to make the thin films. In thick regions near the center, the film appears white. In thin sections near the edge, it appears blue-green. This thickness dependence can be understood in the following way. The film preferentially scatters wavelengths corresponding to the

peak in $I(q)$. In a thin film, only these wavelengths will be scattered to the detector resulting in a structural color. In a thick film, all wavelengths are scattered multiple times and reach the detector.

The sensitivity of the color to the film thickness requires well-controlled casting procedures which increase the cost and limit the coated area. Therefore, for many potential applications it is necessary to eliminate the thickness-dependence. We address this by introducing broadband absorption to the bulk of the films. The absorption length plays a similar role as the thickness: it limits the path length of light through the film by absorbing photons that do not get scattered within a small distance from the surface. Thus, only wavelengths with the strongest scattering will escape the film before being absorbed.

We make a series of thick films with different absorption lengths by drop-casting films with varying concentrations of carbon black. The photo in Figure 2.10a illustrates the effect of adding carbon black on the color of the material. From left to right, the concentration of carbon black, [CB], is increased. Intuitively, one might expect a mixture of black and white to make gray, but here they make blue-green over a range of [CB]. The plot in Figure 2.10b shows the normalized optical scattering spectra for these five samples. As [CB] is increased from 0.02 wt% to 1.80 wt%, the contrast between scattered intensity at the peak and shorter wavelengths is increased, improving the color of the sample. When [CB] = 11.2 wt%, the scattered intensity is reduced by a factor of ten compared to the brightest sample (inset in Figure 2.10b), and the film appears dark gray. The reflectance peak is narrowest for [CB] = 1.80 wt% (Figure 2.10d), and indeed this sample has a distinct blue-green color. Table 2.1 lists the [CB] for each sample and the corresponding extinction length: the extinction length is extrapolated from measurements of aqueous suspensions of CB. Interestingly, the extinction length for sample 3 is 1.3 μm , which is comparable to

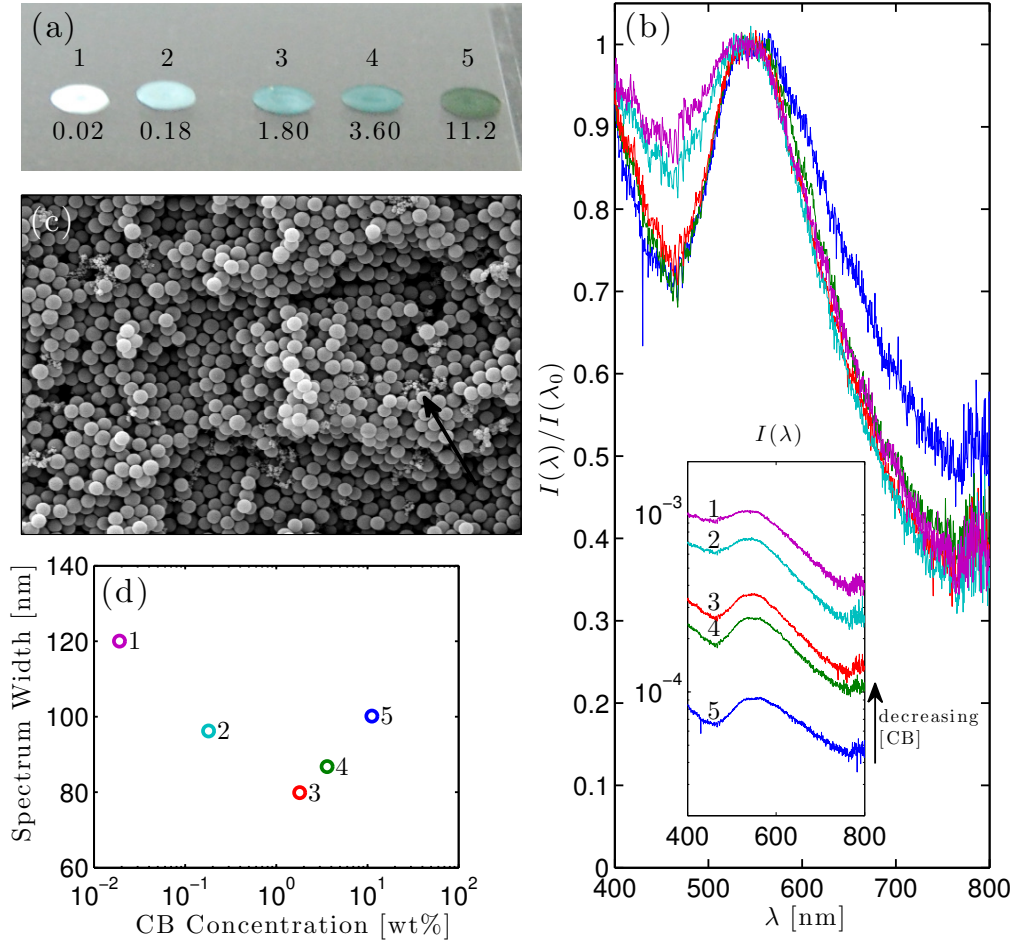


Figure 2.10: *Optimizing color by adding absorption.* a) Photograph of five drop-cast films of 226 and 265 nm PS spheres containing carbon black. Sample numbers and [CB] in wt% appear above and below the samples, respectively. b) Normalized optical scattering spectra recorded at an angle of 20° (experiment geometry shown in Figure 2.12) for the five samples in (a). Inset: Non-normalized scattering spectra for the same samples. c) SEM image of the interior region of sample 3, the field of view is $7.8 \mu\text{m}$ wide, a piece of CB is indicated with an arrow. d) The width of the spectra for each sample in (a) at $I(\lambda)/I(\lambda_0) = 0.90$

the thickness of the thin film pictured in Figure 2.8a.

The carbon black suspension are prepared by mixing Cabot Vulcan XC72R GP-3919 carbon black in DI water at $[CB] = 4.2$ wt% with 1 wt% Pluronic F108 to stabilize the CB. Different volumes of the CB suspension are added to the bidisperse suspensions of spheres to produce samples with different final $[CB]$. To estimate the extinction lengths quoted in Table 2.1 and in Figure 2.10, the transmission spectra of aqueous suspensions of CB are measured using an Ocean Optics USB 650 Red Tide spectrometer. Suspensions ranging from 8×10^{-5} to 2×10^{-2} wt% are used. Measurements are made with three different path lengths: 1 cm, 0.04 cm, and 0.03 cm. The extinction length for all path lengths is proportional to $[CB]^{-1}$, as shown in Figure 2.11, allowing us to extrapolate the extinction length to the $[CB]$ range used in our thick film samples. We use extinction instead of absorption because this measurement does not discriminate between absorbed and scattered light.

Table 2.1: Carbon Black Extinction Length

Sample	$[CB]$ [wt%]	Extinction Length [m]
1	0.02	1.3×10^{-4}
2	0.18	1.3×10^{-5}
3	1.80	1.3×10^{-6}
4	3.60	6.5×10^{-7}
5	11.2	2.1×10^{-7}

The thick films with CB are not iridescent under omnidirectional illumination, but, under directional illumination, the peak wavelength scattered does change slightly when the angle between illumination and detection is varied [15]. Since the colors are the result of single scattering, the position of the scattering intensity maximum does not vary with respect to q , as demonstrated by the spectra in Figure 2.12. The red dots connected by a red line in Figure 2.12 represent the azimuthal average of the SAXS pattern for a sample with the same $[CB]$ prepared on kapton tape. The

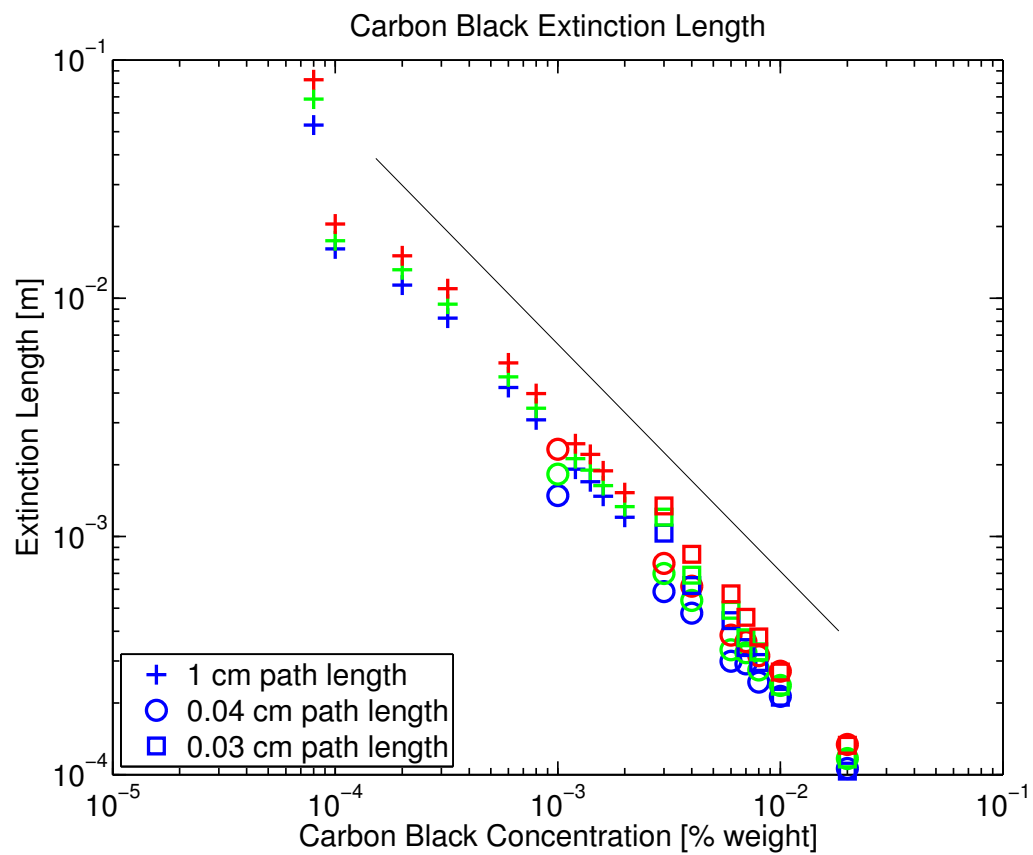


Figure 2.11: *Carbon black extinction length is inversely proportional to the concentration of [CB].*

peaks from the optical and SAXS measurements match when $n_e = 1.29$, implying that $\phi_s = 0.54 \pm 0.05$. The higher value of ϕ_s for the thick films relative to the thin films of the previous section is most likely the result of the different quench-rates used to make the samples. In the spin casting of thin films, the water evaporates within seconds, while water evaporates from the thick films over a few hours, allowing particle rearrangement which leads to a higher ϕ_s . In the thick film, we find that $\xi = 940$ nm, only a few particle diameters.

These isotropic films mimic the essential optical properties of bird feathers that have structural color from isotropic nanostructures. A photograph of an example of these feathers from the crown of *Lepidothrix coronata* is shown in Figure 2.13a, and a transmission electron micrograph (TEM) of the color-producing structure is shown in Figure 2.13b. Normalized $I(q)$ from both *L. coronata* and sample 2 from Figure 2.10 are plotted as a function of q/q_0 in Figure 2.13c. SAXS measurements of the feathers are carried out at beamline 8-ID-I at the APS, Argonne National Labs, as described in Dufresne *et al* [2]. The SAXS patterns reveal similar structures out to the third peak in $I(q)$. Beyond that, the thick film has additional peaks that arise from the uniformity of the spheres used in the sample. We compare the performance of the feathers and films by plotting optical scattering spectra for both at 20° in Figure 2.13d. The scattered optical intensity peak for *L. coronata* is narrower than the film: the full-width at $I(\lambda)/I(\lambda_0) = 0.90$ is 49 nm for the feather and 82 nm for the film. Similarly, *L. coronata* has a narrower first peak in $I(q)$. *L. coronata* also displays less scattering at shorter wavelengths. This may be due to a significant difference in the two structures: the feathers have spheres of air in a high-index of refraction background whereas the films have spheres of a high-index in a background of air.

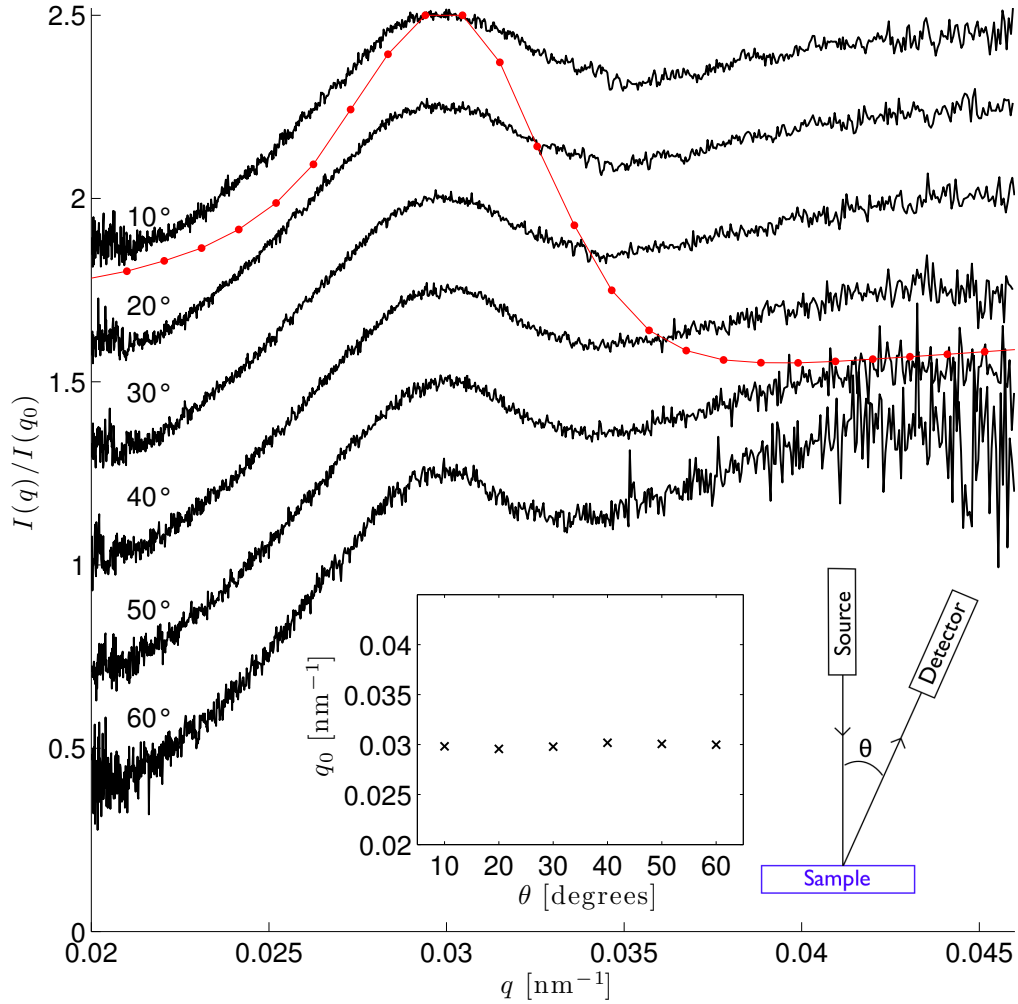


Figure 2.12: *Color is the result of single scattering.* Normalized reflectance spectra taken over a range of angles and converted to q -space for sample 2 in Figure 2.10 (black lines), and the azimuthal average of the SAXS pattern for a similar sample (red dots). The spectra have been vertically offset for clarity. *Inset:* Position of the peak as a function of angle. *Schematic:* the source and sample are fixed and the detector is rotated.

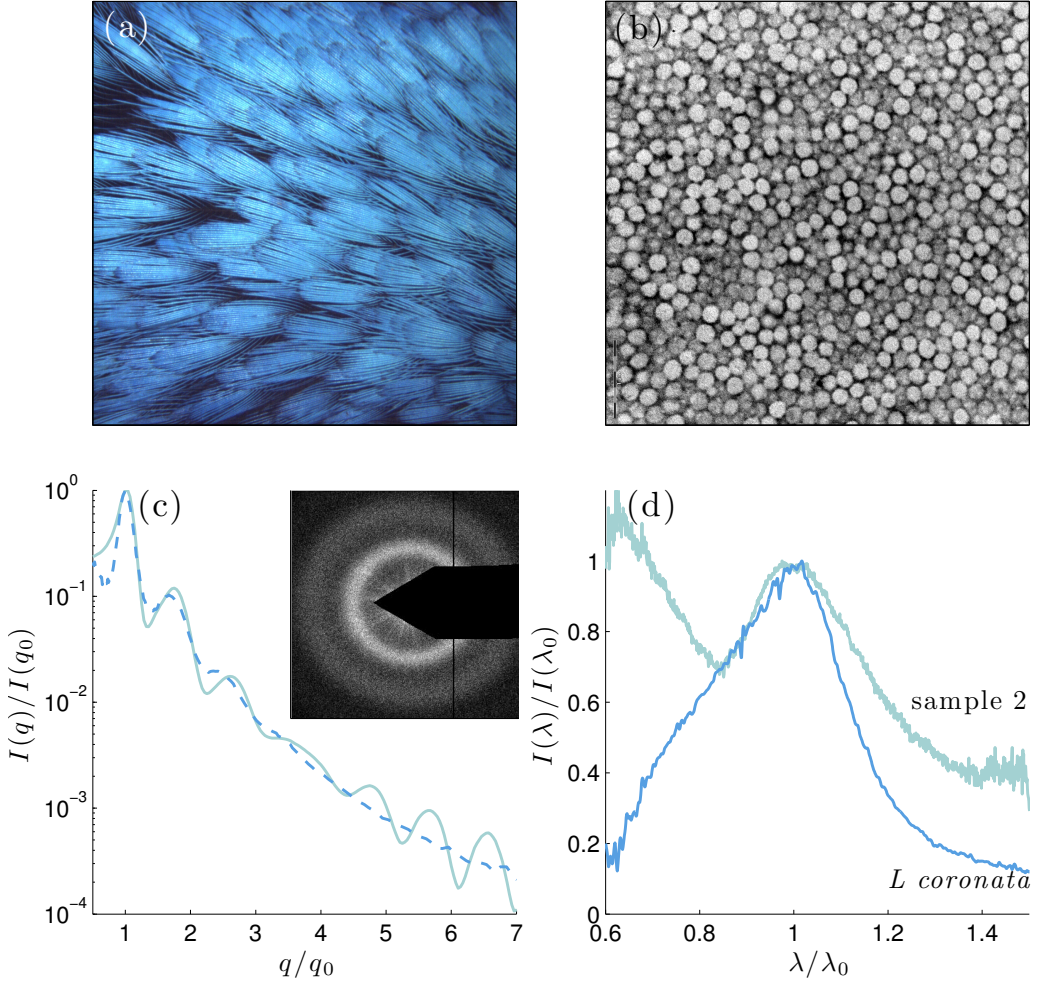


Figure 2.13: *Comparison with feathers.* a) Photograph of crown feathers from *L. coronata*, the field of view is 1 cm. b) TEM image of air spheres in beta-keratin from *L. coronata*, the field of view is 5.5 μm . c) Azimuthal averages from SAXS measurements of *L. coronata* (dashed line) and a thick film with the same [CB] as sample 2 in Figure 2.10 (solid line). *Inset:* SAXS pattern from *L. coronata*, the field of view is 0.14 nm^{-1} and the gray values are logarithmic in intensity. d) Comparison of optical scattering data taken at an angle of 20° (experiment geometry shown in Figure 2.12) from *L. coronata* and sample 2 from Figure 2.10. The line colors correspond to the apparent color of the feathers and the thick film.

Chapter 3

Dumbbell Crystals

3.1 Anisotropic Particles: Colloidal Molecules

Nanoscale colloidal particles with anisotropic interactions, or *colloidal molecules*, are expected to enable a wide range of materials with novel optical and mechanical properties [35]. However, robust and flexible processes for synthesizing large quantities of uniform nanoparticles with a variety of controlled shapes and interactions are only beginning to emerge [18, 3, 19, 17, 16]. With particles in hand, their self-assembly presents new challenges. While the self-assembly of spherical particles into periodic structures is relatively robust and well-characterized, anisotropic particles introduce additional degrees of freedom which complicate the formation of long-range periodic structures [36, 37, 38]. In this chapter, I describe the formation of large crystals of optical scale dumbbells by electric-field assisted self-assembly and characterize their structural and photonic properties. We demonstrate that dumbbell crystals display desirable properties associated with both photonic and liquid crystals. Furthermore, we perform numerical simulations of self assembly that highlight the critical importance of external fields in crystallizing even simple anisotropic particles.

This work is enabled by a synthesis technique developed in our lab which is described in Ref. [3] and also in Appendix A. Using this technique, we synthesize large quantities of monodisperse polymer dumbbells at optical length scales. Briefly, we start with a suspension of monodisperse polystyrene spheres and swell them with a mixture of styrene and trimethoxysilylpropylacrylate. Upon polymerization, these particles develop a spherical core-shell structure and form dumbbells after another swelling and polymerization step. The relative sizes of the two lobes can be controlled by varying the amount of monomer used in each step [39]. The particles we use here have two lobes of the same size, with a diameter of 267 ± 5 nm, and an overall length of 422 ± 7 nm, giving them a length-to-diameter ratio, $\alpha = 1.58$.

3.2 Dumbbells Crystallize Only Under Strong Confinement

While these dumbbells readily crystallize in confined films [3], they resist crystallization in the bulk. As the film thickness increases, dumbbells form ordered monolayers laying down, ordered monolayers standing up, as shown in Figure 3.1a, and three variations of ordered bilayers (down/down, down/up and up/up) [3]. However, when these dumbbells are dried into a film of even three layers, they pack randomly, as shown in Figure 3.1b. These observations are at odds with numerical simulations predicting the equilibrium phase diagram of hard dumbbells, which suggests that these particles should form structures with long-range order in thermodynamic equilibrium at these volume fractions [40].

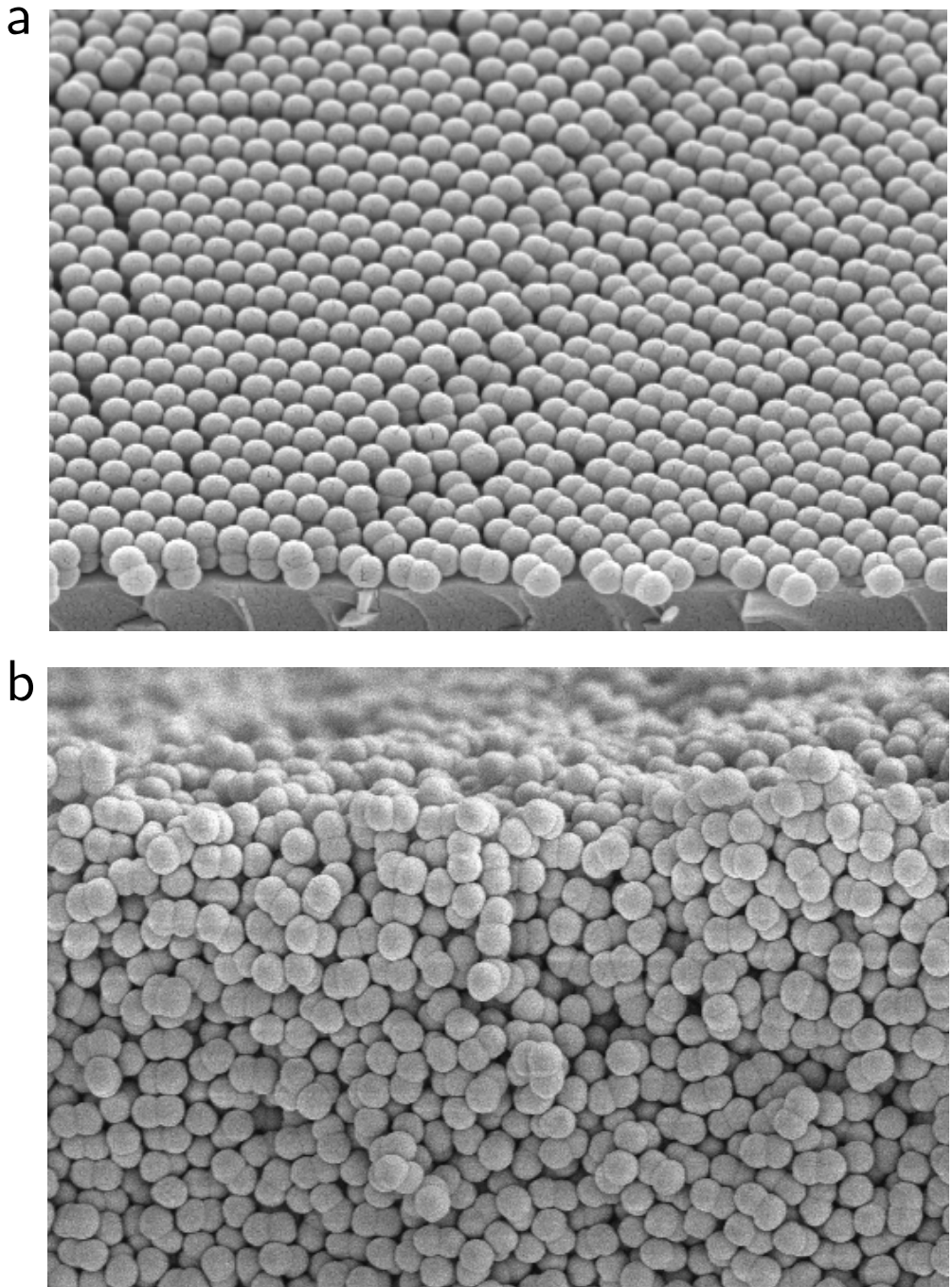


Figure 3.1: *Dumbbells crystallize in confinement, but not in the bulk.* a), SEM image of dry dumbbells cast into thin films by vertical deposition. Dumbbells form ordered mono- and bi-layers [3]. b), SEM image of dumbbells cast into an amorphous thick film. The fields of view in (a) and (b) are 7.6 μm across.

3.3 Electric-Field Assisted Crystallization

To adopt a crystalline packing, dumbbells not only have to arrange themselves on a periodic lattice, but also have to orient themselves in a specific direction. In order to facilitate crystallization, we bias the particle orientations with an external electric field [41, 42, 43]. The anisotropic polarizability of dumbbells causes them to align themselves with the direction of the electric field. The applied electric field also introduces long range interactions between particles which tend to locally concentrate the suspension [44, 45, 46, 47]. In Figure 3.3, we demonstrate the capability to control the structure of dumbbell suspensions with an external electric field. With no applied electric field, the suspension is strongly scattering with no structural color or birefringence. Initially, the sample is gray when viewed under crossed polarizers because the random orientations and positions of the dumbbells act to mix the polarization of light propagating through the sample. We then apply an AC electric field ($f = 50$ kHz, $E = 1040$ V/cm) with co-planar gold electrodes separated by a 0.85 mm gap in a 20 μm thick glass sample chamber, a schematic of the chamber is shown in Figure 3.2. The sample cell is placed between crossed polarizers, which are at an angle of approximately 45 degrees to the field direction. Digital color movies are recorded on an inverted Axiovert 200 Zeiss microscope using a digital SLR camera (Canon-EOS Digital Rebel T1i). About six seconds after the field is turned on we see a wave of birefringence originating from the electrodes, where the electric field strength is highest. Within 36 seconds, there is strong birefringence and structural color visible throughout the bulk. The patchwork of structural color across the sample points to polycrystalline domains on the order of 7 microns in width. The crystallites can be further compacted by a step change in the frequency of the applied electric field (from 50 to 10 kHz), which can be seen in Supplementary

Movie 2 of Ref. [4], which changes the form of the interparticle dipole interaction [47]. When the electric field is turned off, structural color and birefringence rapidly disappear. We quantify the difference in on and off rate by plotting the ratio of the intensity in the red channel to the total intensity of Supplementary Movie 1 of Ref. [4] in Figure 3.4. Field-switchable photonic crystals have previously been demonstrated with spherical particles [48], but suspensions of dumbbells may offer more flexibility and speed.

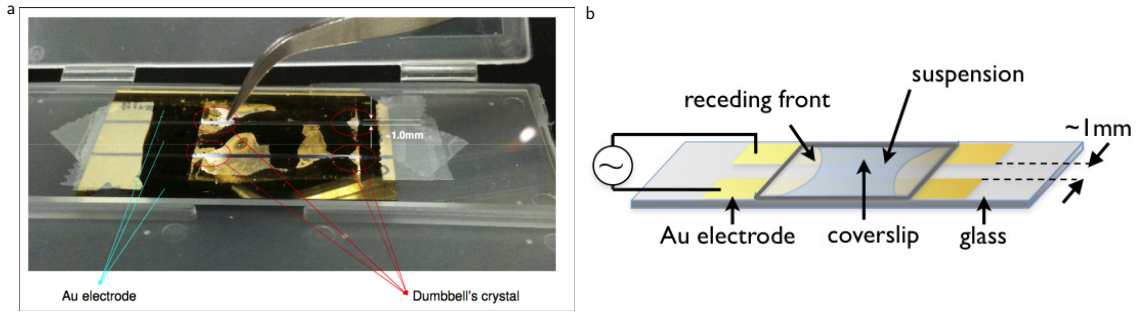


Figure 3.2: *Sample chamber details.* a), Photograph of the sample chamber used to make dumbbell crystals. b), Schematic of the sample chamber.

To assemble stable crystalline packings, we dry dumbbell suspensions in the presence of an electric field. The crystal seen in Figure 3.5a is approximately one hundred particles thick, and is the result of the application of an AC electric field ($f = 50$ kHz, $E = 1040$ V/cm) during the unidirectional drying of an aqueous suspension of dumbbells with initial volume fraction, $\phi = 0.13$ [41]. Additional SEM images of the resulting structures can be seen in Figure 3.6 - 3.9. Previous studies have used magnetic fields to align ellipsoidal particles during convective assembly but were only able to achieve crystal thicknesses of approximately 20 particle layers [49].

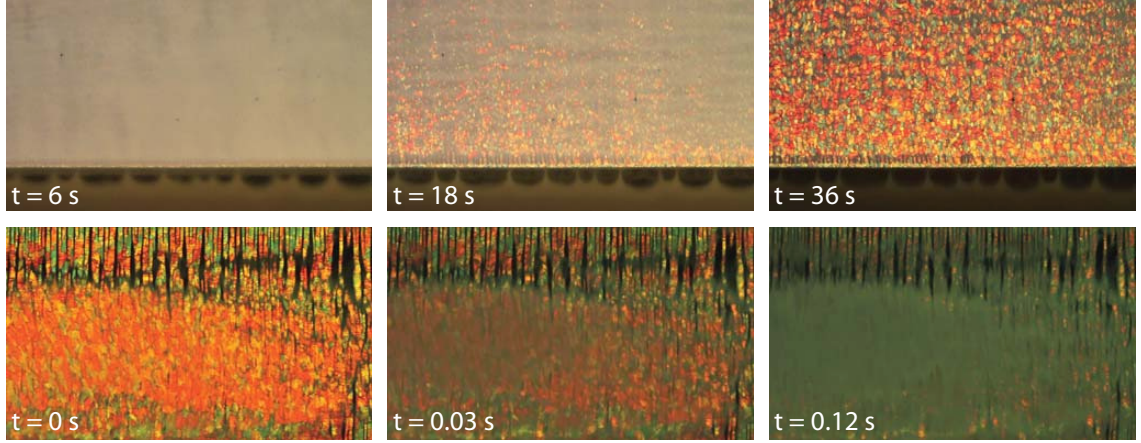


Figure 3.3: *Aqueous suspensions of dumbbells display reversible crystallization in AC electric fields.* Aqueous suspension of dumbbells at volume fraction $\phi = 0.13$. *Top row*, Snap shots showing the onset of crystallization in an aqueous suspension of dumbbells in an AC electric field. The dark stripe across the bottom of the frame is a gold electrode. The sample is imaged through crossed polarizers. *Bottom row*, Snap shots showing the rapid loss of structural color and birefringence when the electric field is turned off. The whole process can be seen in Supplementary Movie 1 of Ref. [4]. The field of view in each image is 1.4 mm across.

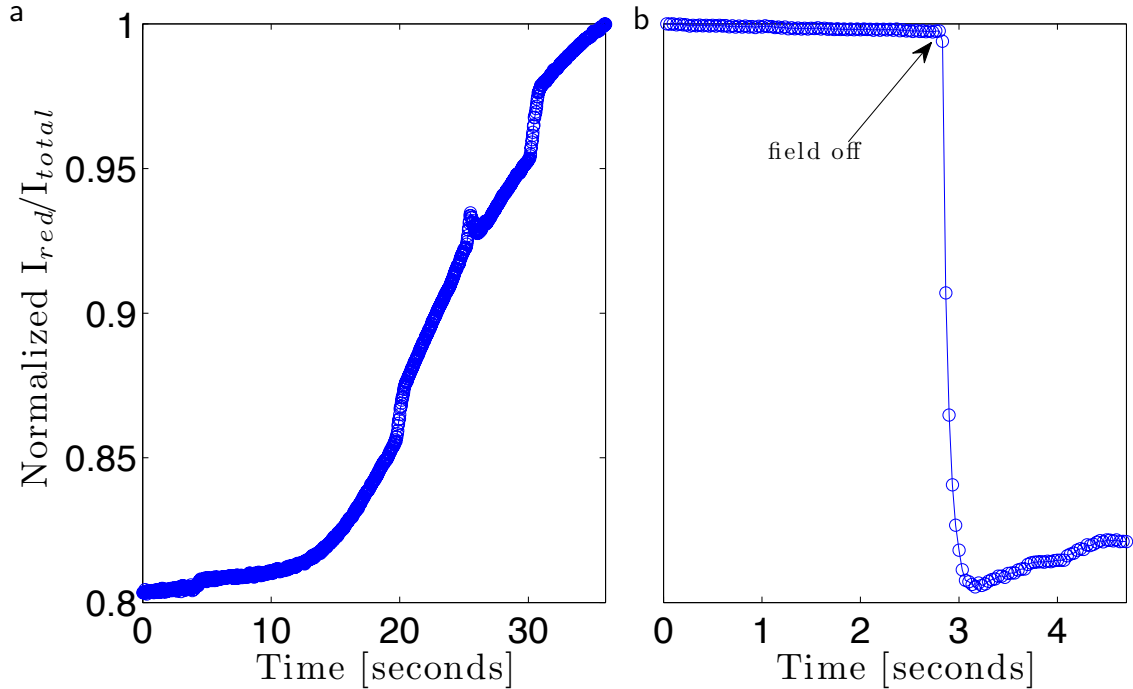


Figure 3.4: *The timescales for the onset and disappearance of structural color and birefringence are very different.* Ratio of the intensity in the red channel to the total intensity from the video of *a)* crystal formation and *b)* crystal melting.

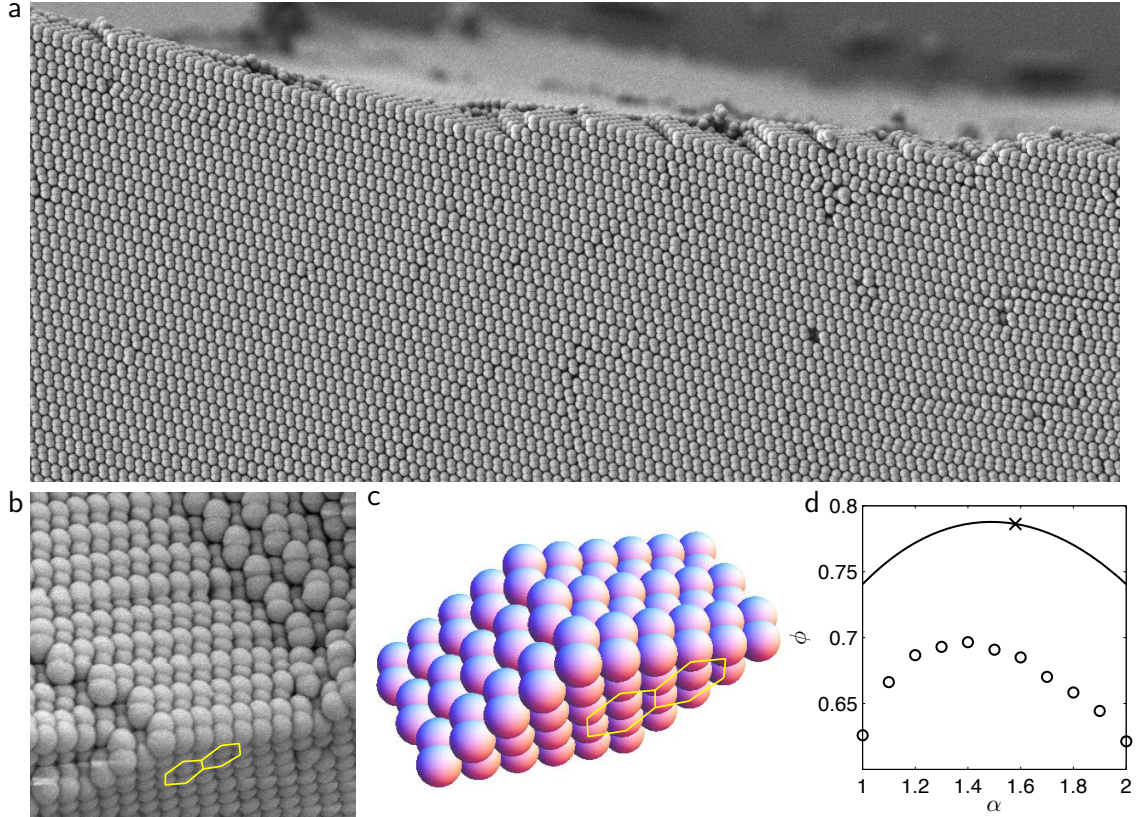
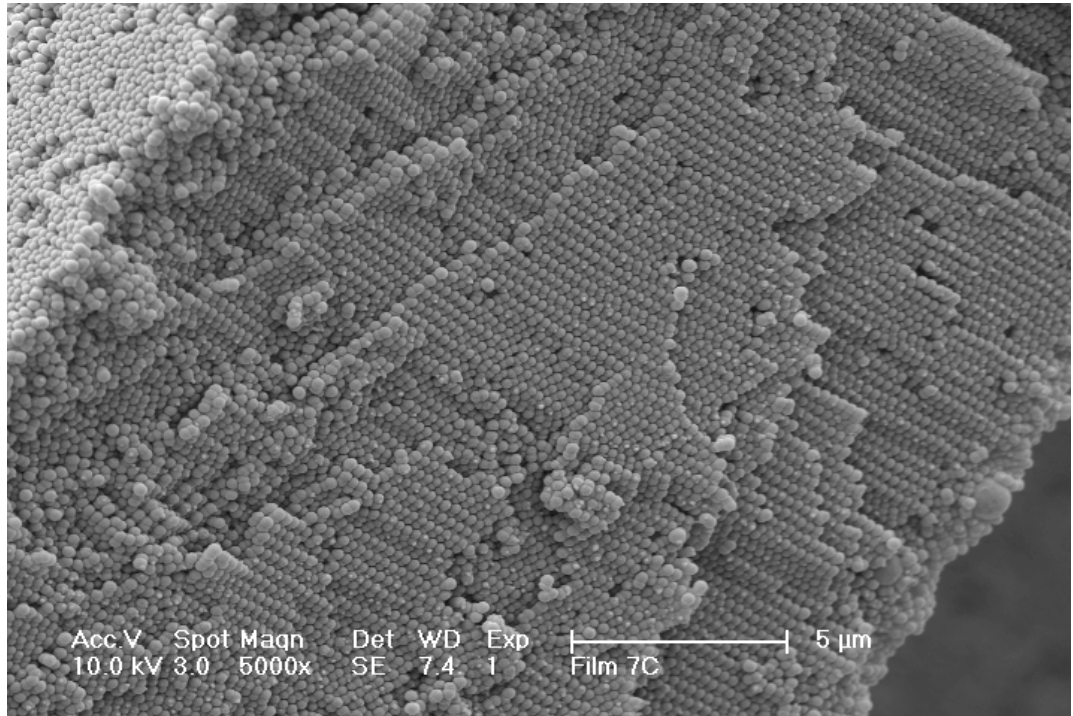


Figure 3.5: *Crystal structure of suspension dried in an AC electric field.* a), SEM image of crystal formed by drying a suspension of dumbbells in the presence of an electric field. In this image, the electric field orientation is approximately vertical and the direction of flow due to drying is from right to left. The field of view is $27\text{ }\mu\text{m}$ across. b), SEM image highlighting crystal structure. Two adjoining hexagons formed by the dumbbell lobes are highlighted by the yellow hexagons. The field of view is $3.6\text{ }\mu\text{m}$ across. c), Model of the crystal structure suggested by SEM images. Two adjoining hexagons are highlighted and correspond to the highlighted facet in (b). d), Packing fraction versus aspect ratio for crystalline structures (line) and random, jammed packings (circles) generated from numerical simulations described in the methods section. The packing fraction for the aspect ratio 1.58 dumbbells in a crystalline structure is $\phi = 0.7862$ (x).

a



b

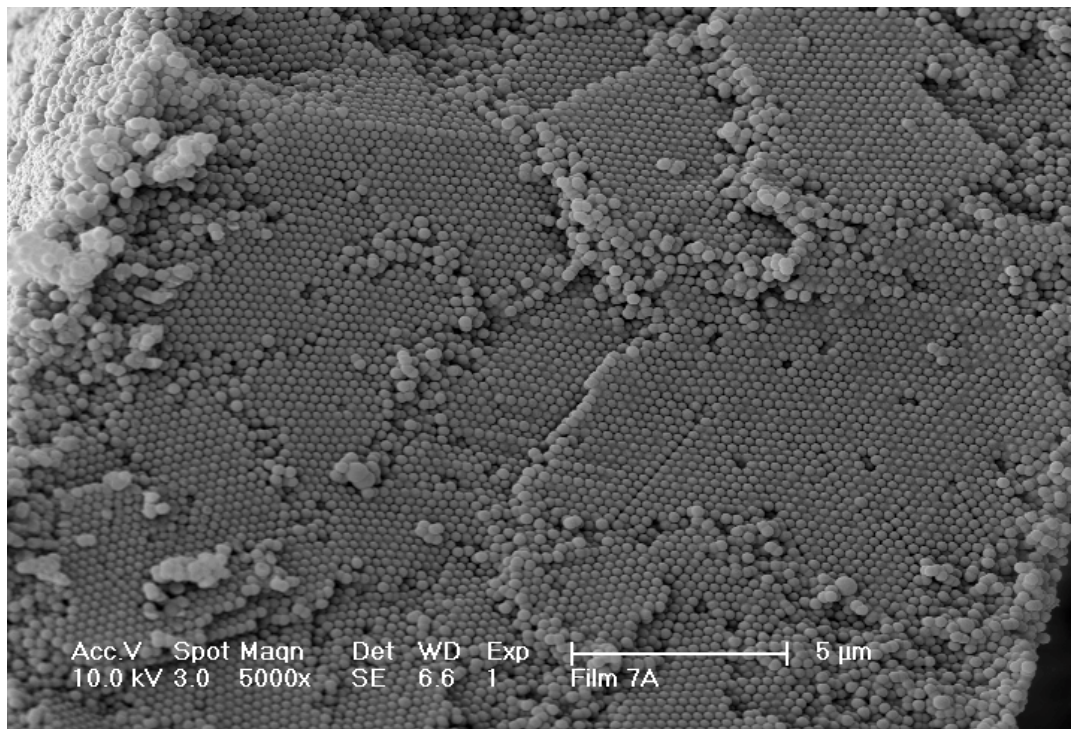


Figure 3.6: *SEM images showing different cross-sectional views of a dumbbell crystal. a), The electric field direction relative to this image is approximately from bottom left to top right. b), The electric field direction relative to this image is approximately into the page.*

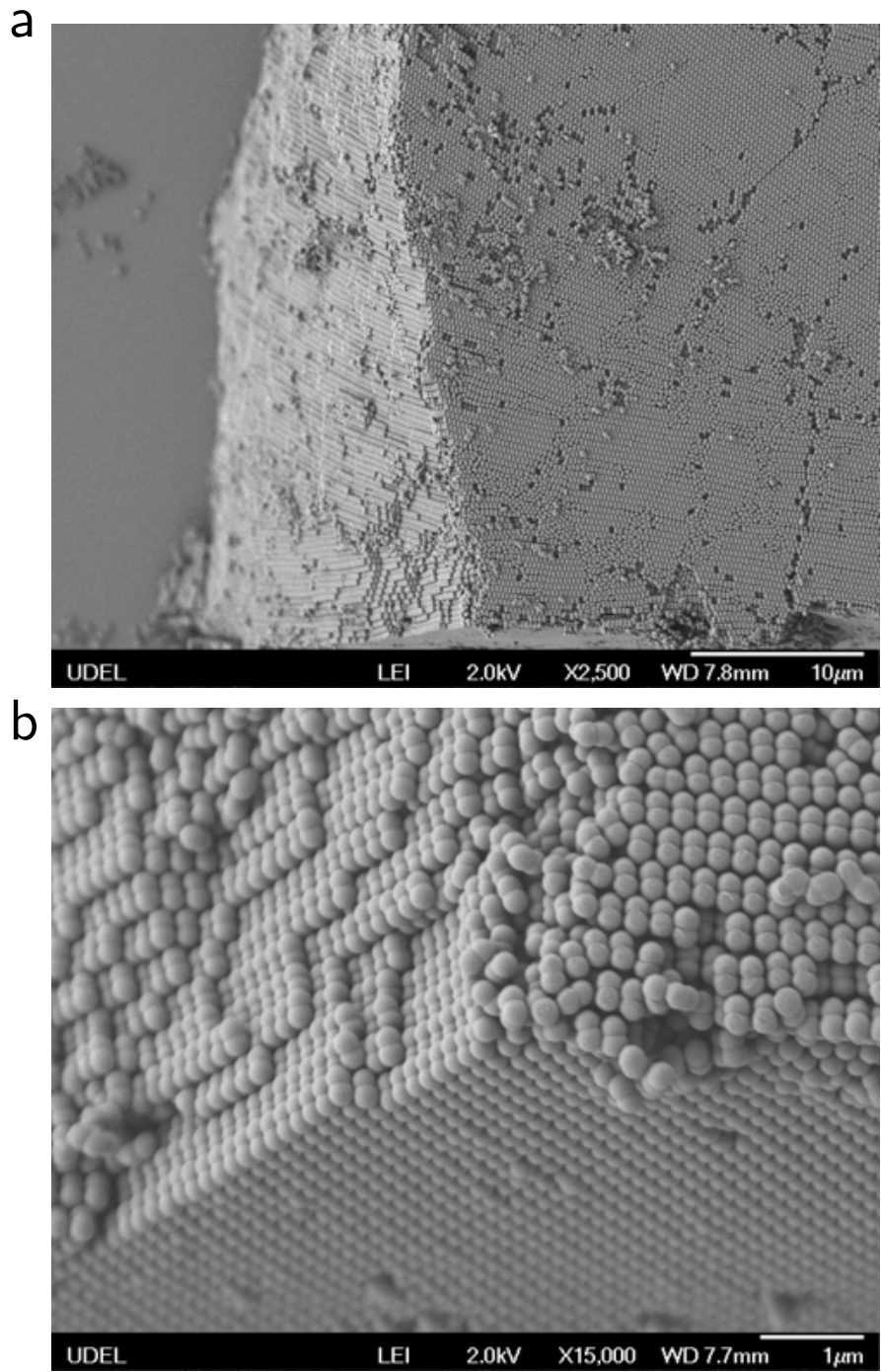


Figure 3.7: SEM images showing details of a dumbbell crystal. a), The electric field direction relative to this image is approximately vertical. b), The electric field direction relative to this image is approximately vertical.

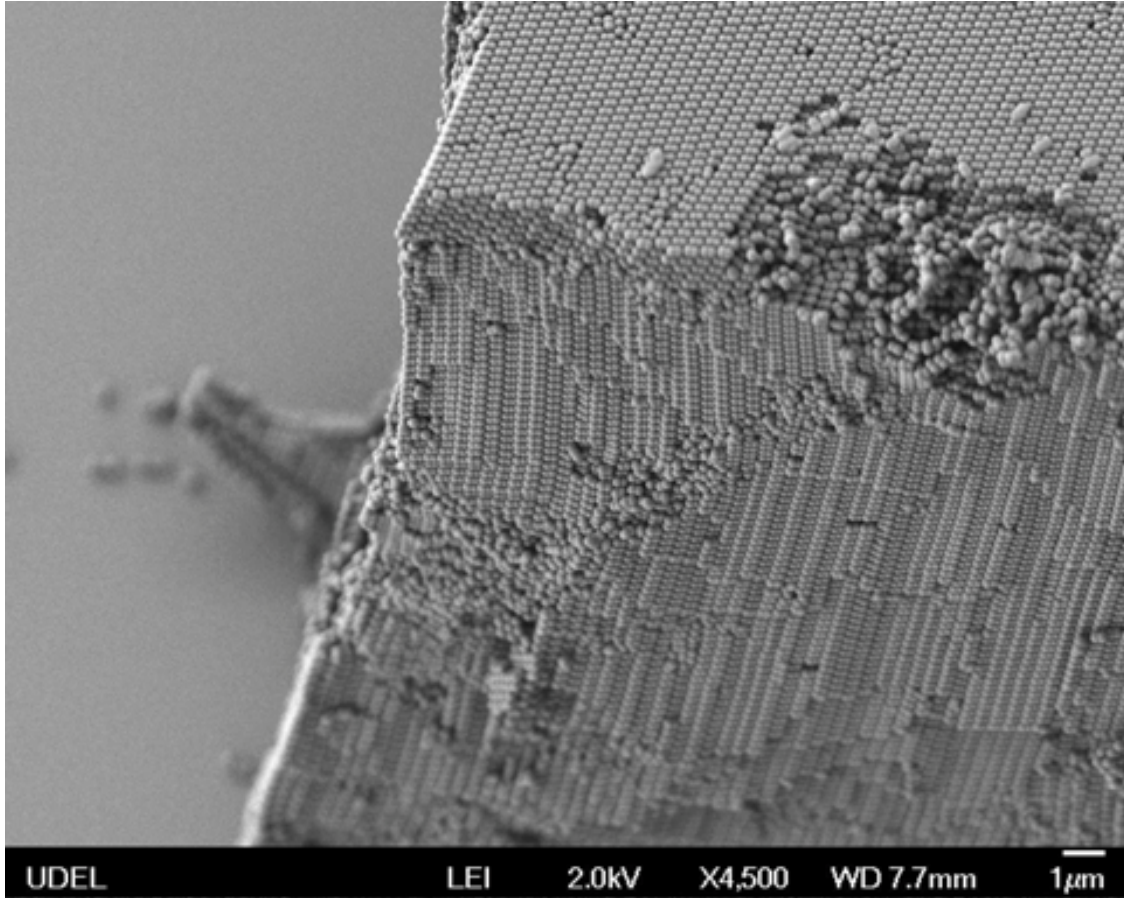


Figure 3.8: SEM image of a dumbbell crystal. The electric field direction relative to this image is approximately horizontal.

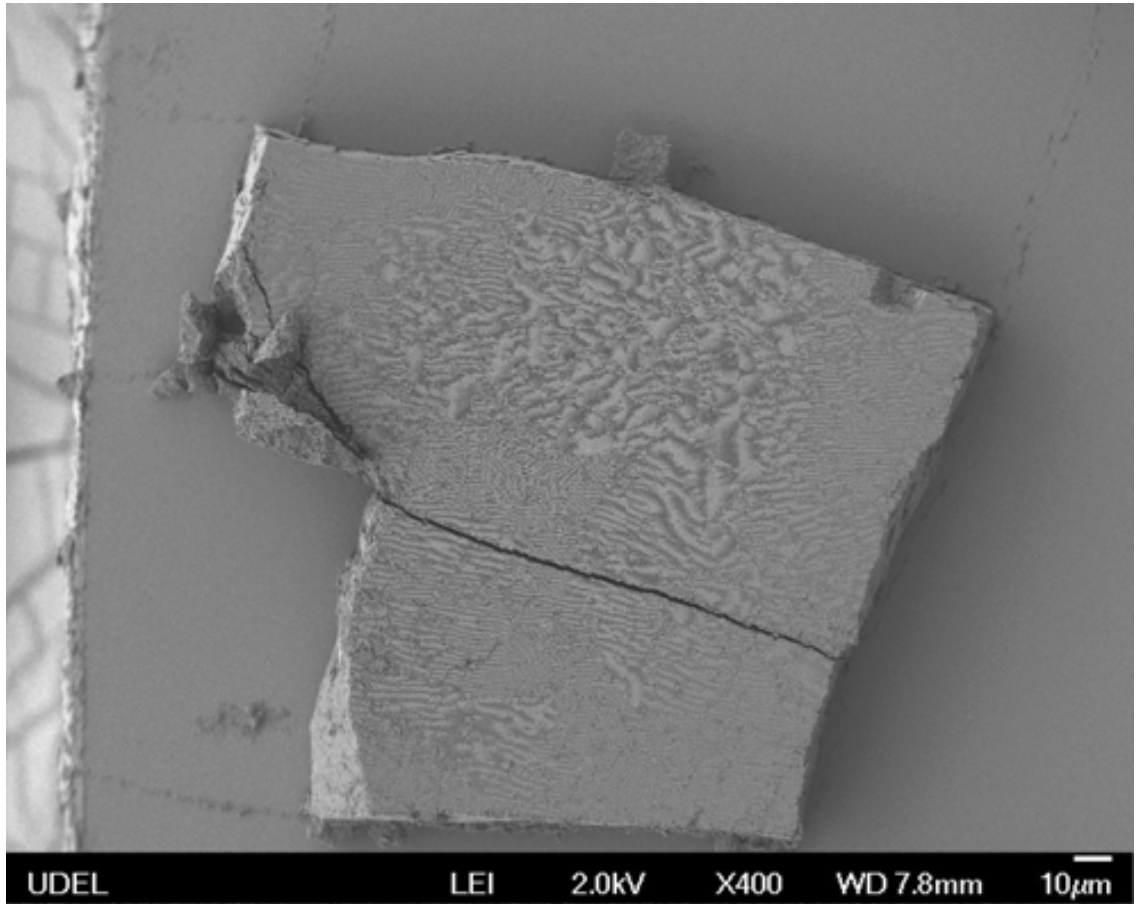


Figure 3.9: *SEM image of a dumbbell crystal.* Low magnification SEM image of a dumbbell crystal. The Moire fringes in the image indicate that there is long-range order in the sample.

3.4 Structural Properties of Dumbbell Crystals

The crystal structure formed by dumbbells is more complicated than the cubic structures formed by spherical particles. SEM images of the dumbbell crystals reveal a number of features that allow us to identify the structure. In the bottom of Figure 3.5b one can see lobes of the dumbbells in hexagonally-packed layers, highlighted by yellow hexagons, with the major axis of the dumbbells tilted relative to the normal of these planes. Successive layers pack such that the hexagonally-packed bottom lobes of a new layer fit into the hexagonally-packed top lobes of the previous layer. This layering scheme allows for successive layers to fit snugly together for any particle tilt, so long as the top and bottom lobes of each particle can remain in contact with the top and bottom lobes of its six nearest neighbors. For ordered close-packed spheres, there are three possible translational alignments of one hexagonally packed layer with respect to the next, which specify the familiar FCC, HCP and RHCP packings. Dumbbells have an additional three-fold orientational degeneracy, due to the tilting of the particles within each layer. However, in an applied electric field, the dumbbells tend to maintain a constant orientation from plane to plane, as shown in Figure 3.5a,b. A schematic of this packing is shown in Figure 3.5c. During drying, capillary forces tend to drive suspended particles toward their densest packing. To our knowledge, this packing, which was found to be equilibrium structure of hard dumbbells [40] is the densest packing of symmetric dumbbells. In numerical simulations, we have verified that this packing is mechanically stable and at least a local maximum in the packing density, as described in Figure 3.10.

These structures have very high packing fractions. For the dumbbells used in our experiments, the packing fraction is $\phi = 0.7862$. This packing fraction is significantly higher than both the densest crystalline sphere packing, $\phi_{sphere}^{FCC} = 0.7405$, and the

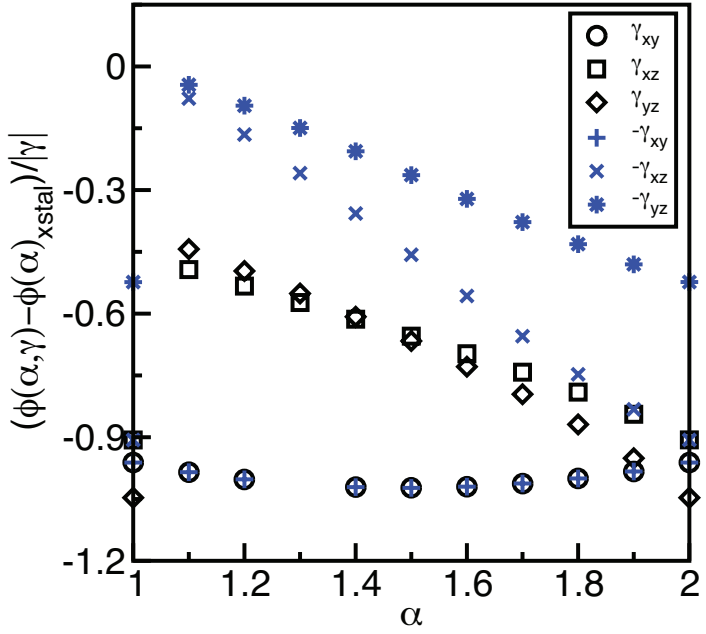


Figure 3.10: The crystalline dumbbell structure described here is at least the densest local structure with respect to all possible linear strains of the cubic boundary. To show this, we first create a mechanically stable crystalline packing by initializing the system with crystal positions and orientations and then apply the isotropic compression protocol to relax it. We obtain packing fractions $\phi_J \approx \phi_{xstal} + 10^{-8}$, which is consistent with the fact that the stopping criterion allows infinitesimal overlaps with $V/N\epsilon \approx 10^{-16}$. We then perturb the box shape using three orthogonal infinitesimal strains γ_{xy} , γ_{xz} , and γ_{yz} in both the positive and negative strain directions, and use the isotropic compression protocol at fixed strain to find the nearest mechanically stable packing with $\phi_J(\gamma)$. The packing fraction decreases, $\phi_{xstal} - \phi_J(\gamma) < 0$ for all aspect ratios and perturbations we studied.

densest known crystalline packing of ellipsoids, $\phi_{ellipsoid} = 0.7707$ [50]. Figure 3.5d shows the anticipated packing fraction of dumbbells in this crystal structure as a function of aspect ratio,

$$\phi = \frac{(3 - \alpha)\alpha^2}{2 + (\alpha - 1)\sqrt{6 - 2(\alpha - 1)^2}} \phi_{sphere}^{FCC}. \quad (3.1)$$

The aspect ratio that gives the highest packing fraction is 1.5, with $\phi = 0.7877$. The dumbbell tilt angle for the crystal structure depends on aspect ratio, as shown in Figure 3.11. For aspect ratios 1.5 and 1.58, the tilt angles for the crystal structure are 16.8 and 19.5 degrees, respectively.

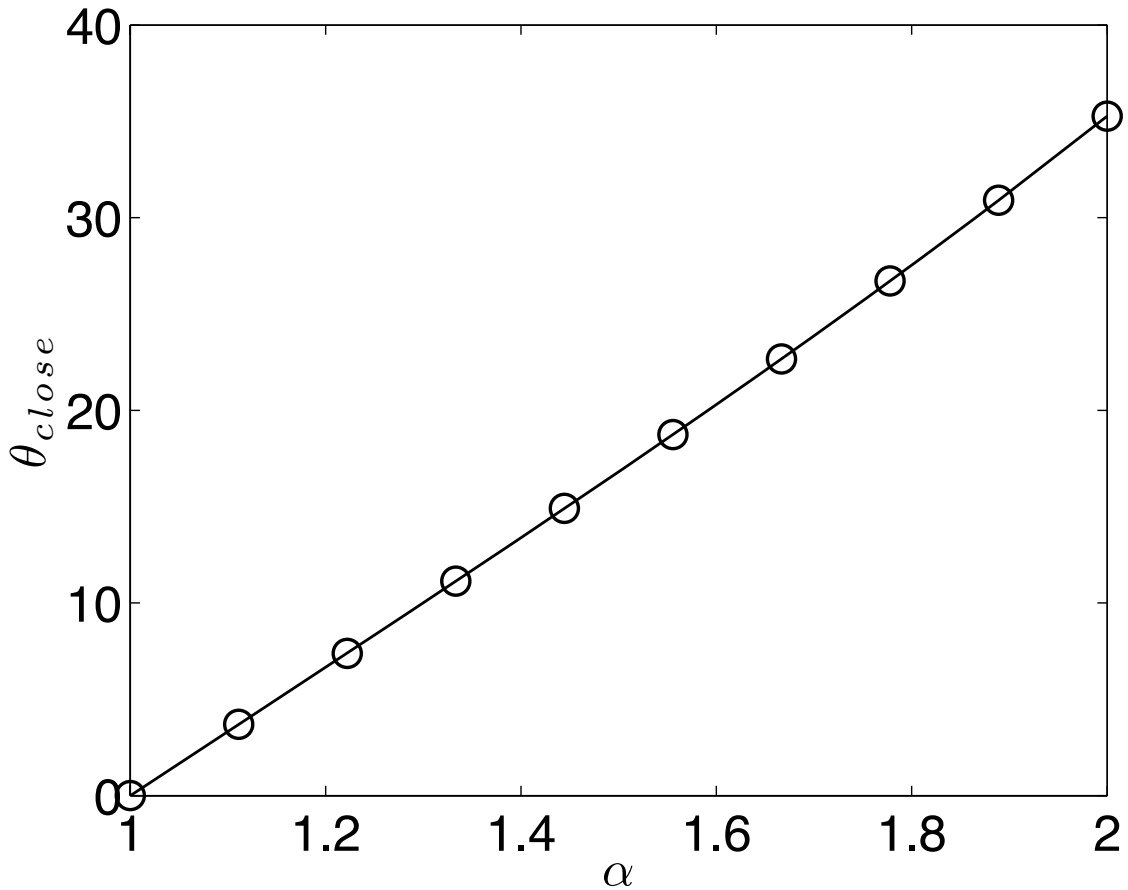


Figure 3.11: Angle of dumbbell tilt that corresponds to the maximum packing fraction as a function of dumbbell aspect ratio, α .

Our experiments suggest that restricting the orientation of the dumbbells is critical to achieving crystallization – numerical simulations of the jamming of dumbbells under compression yield similar findings. We perform numerical simulations of mechanically stable dumbbell packings by successively compressing and decompressing the system and relaxing the energy until all forces are balanced and inter-particle overlaps are vanishingly small [51]. The probability of the system crystallizing as a function of aspect ratio α for slow thermal quench rates is plotted in Figure 3.12. In the absence of an external field that favors alignment, systems of dumbbells with α higher than 1.1 have essentially zero probability of crystallizing at the quench rates explored here. By contrast, restricting particle orientations dramatically increases the probability of crystallization. In that case, the probability of crystallization is highest for aspect ratios between 1.2 and 1.6. Previous Monte Carlo simulations predict that the crystalline phase we observe should be thermodynamically stable for α greater than 1.3 even in the absence of an external field [52]. However, in our simulations in the absence of the field, the particles form amorphous mechanically stable packings at densities that are systematically lower than their crystalline counterparts as plotted in Figure 3.5d, and also lower than random jammed packings of oblate ellipsoids [50, 53]. We find that lowering the quench rate used in our simulations by a factor of 1000 does not have a significant effect on the probability of crystallization for either the aligned or unrestricted dumbbells, as seen in Figure 3.12. We perform extensive numerical simulations of soft dumbbell particles composed of two rigidly-constrained spheres. The interactions between dumbbell particles arise from purely repulsive, pairwise linear spring forces that act centrally between the centers of the spheres that comprise two different dumbbells. We generate mechanically stable dumbbell packings via isotropic compression—by successively compressing and decompressing the system and relaxing the energy until all forces and torques are balanced.

anced and inter-particle overlaps are vanishingly small using the algorithm described in detail in [51]. To create the amorphous mechanically stable dumbbell packings described in Figure 3.5d, we initialize the system in a dilute state at packing fraction $\phi_0 = 0.2$ with random dumbbell positions and orientations inside a unit cube. We choose the increment in packing fraction as $\Delta\phi \leq 10^{-4}$ and the final potential energy $V/\epsilon N$ of the packing to be in the range $10^{-16} < V/\epsilon N < 2 \times 10^{-16}$, where ϵ is the characteristic energy scale of the repulsive interaction and $N = 512$ is the number of dumbbells. We also perform simulations to compare the probability to form a crystalline structure in the presence and absence of a strong aligning field as shown in Figure 3.12 in systems ranging from $N = 27$ to 125 particles. We thermally quench equilibrated fluid systems at $\phi_0 = \phi_{xstal} - 0.2$ and $k_b T/\epsilon = 10^{-3}$ by linearly decreasing the temperature to $T = 0$ over a wide range of thermal quench rates $10^{-2} > rk_b T \tau / \epsilon > 10^{-9}$ to generate the initial configurations, where τ is a typical collision time between dumbbells. In Figure 3.12, we show results for $rk_b T \tau / \epsilon = 10^{-6}$ and $rk_b T \tau / \epsilon = 10^{-9}$ since these rates yield FCC packings for spheres. We then use the isotropic compression protocol described above with initial configurations from the thermal quenches to generate dumbbell packings. To simulate a strong aligning field, the orientations are initially chosen to be consistent with the crystalline packing at each aspect ratio, and then prevented from evolving during the thermal quench and isotropic compression packing algorithm. The fraction of crystalline packings P_{xtal} is determined as the ratio of the number of packings with $|\phi_{xstal} - \phi_J| < 10^{-6}$ to the total number of trials.

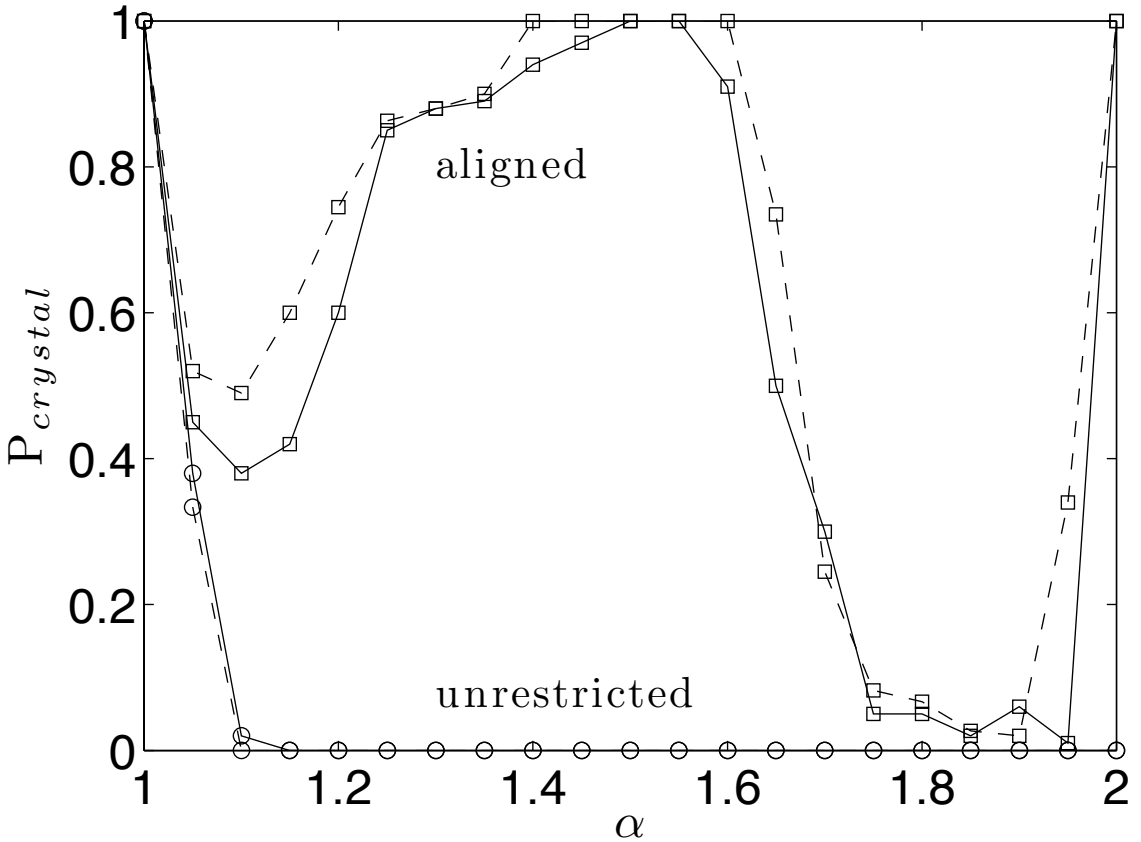


Figure 3.12: *Simulations demonstrate crystal formation depends strongly upon control of dumbbell orientation.* Probability of crystallization for a system of dumbbells as a function of aspect ratio. Systems with aligned dumbbells (squares) have significant probabilities of crystallization for most aspect ratios. Systems with unrestricted dumbbell orientations (circles) have near zero probabilities of crystallization for aspect ratios greater than 1.1. Each point is the result of 100 independent simulations. The two line types represent simulations performed with different quench rates, the dashed line has a quench rate that is 1000 times lower than the solid line.

3.5 Photonic Properties of Dumbbell Crystals

These dumbbell crystals have partial photonic band gaps. Figure 3.14a shows a normal incidence reflection spectrum of a $70 \mu\text{m} \times 70 \mu\text{m}$ area of a dumbbell crystal measured with a Nikon Optiphot 66 Microscope in epi-scopic mode. We use a 40X objective lens for illumination and collection of reflected light, and use a field stop to reduce the size of the illumination and collection area. The reflected light is transferred to an Ocean optics HR2000+ spectrometer through an optical fiber and normalized to the spectrum recorded from an Ocean Optics reflection standard. We see a strong peak in the reflectance at 644 nm with a full width at half maximum (FWHM) of 72 nm. Using our model of the crystal structure, we calculate the photonic band structure. These calculations show partial band gaps in certain crystal directions, as described in Figure 3.13. In the direction optical reflection was probed (Figure 3.14a), the predicted photonic band gap is centered at 660 nm with a FWHM of 30 nm. The center wavelength matches well that of the reflection peak in Figure 3.14a, but the width is significantly smaller. We believe the presence of multiple domains with different crystal orientations, as seen in the SEM images, leads to a spectral broadening of the reflectance peak.

In addition to having a photonic band gap, these dumbbell crystals are birefringent. To visualize the birefringence, we image the crystals through crossed polarizers using wavelengths inside and outside the band gap (650 and 534 nm). For both wavelengths, we observe a sinusoidal modulation of the transmitted intensity with the relative angle of the sample and crossed polarizers, as seen in Supplementary Movies 3 (650 nm) and 4 (534 nm) of Ref. [4]. The depth and phase of the modulation varies from location to location within the sample, as shown in Figure 3.14b,c and Figure 3.15. Depolarization of transmitted light inside the band gap is expected from

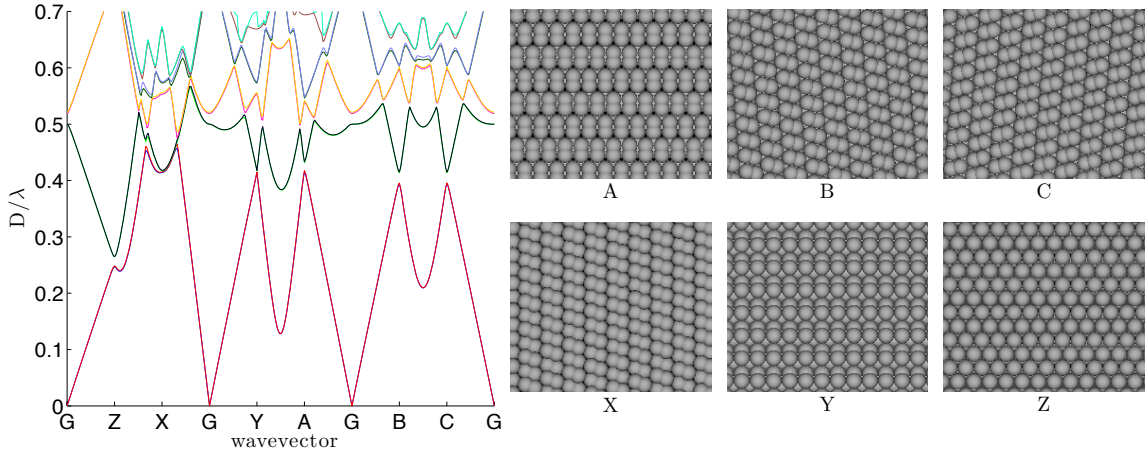


Figure 3.13: *Photonic band structure.* *Left panel:* Photonic band structure, where D is the diameter of one dumbbell lobe, 267 nm for the dumbbells we use. *Right panel:* Illustrations corresponding to the crystal orientations for each wave vector.

the previous studies of colloidal crystals due to the polarization-dependent efficiency of Bragg diffraction from the crystal structure [54]. In contrast, we also observe strong birefringence outside of the photonic band gap, where crystals of colloidal spheres would not be birefringent. Since this light is not diffracted by the crystal's Bragg planes, we believe that the birefringence originates from the anisotropic shape of individual dumbbell particles. The images of transmitted intensity during the rotation of crossed polarizers in Figures 3.14b,c and 3.15 are recorded on a Nikon TE-2000 inverted optical microscope with a Photron FASTCAM 1024 PCI camera. The halogen bright field lamp on the microscope is used for illumination and colored filters are used to select wavelengths inside and outside the photonic band gap.

Anisotropic colloidal particles can self assemble into crystalline structures with long-range order in the presence of an external field. Crystals of anisotropic particles have novel optical properties which combine photonic band gaps with birefringence. Furthermore, anisotropic particles could improve the speed and functionality of field-switchable photonic crystals by allowing dramatic changes to optical properties through mere particle reorientation and not complete reorganization of the

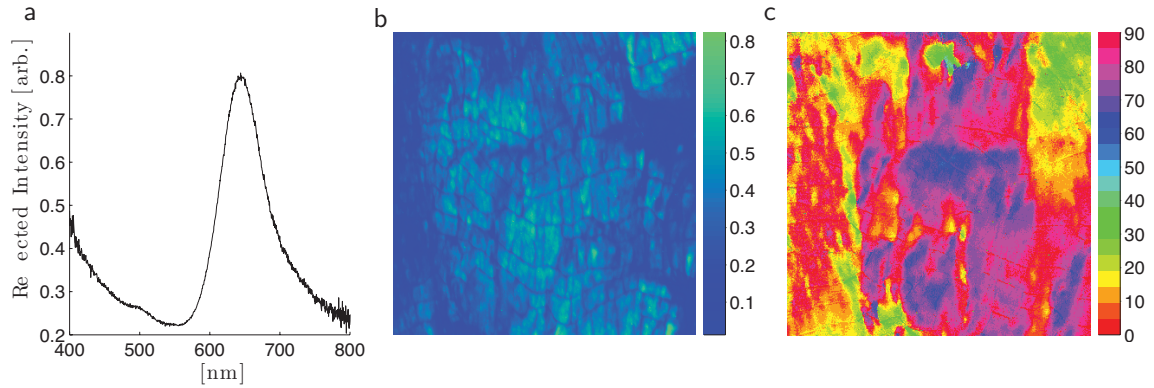


Figure 3.14: *Dumbbell crystals have a partial photonic band gap and are birefringent.*
 a), Normal incidence reflection spectrum from a $70 \mu\text{m} \times 70 \mu\text{m}$ area of a dumbbell crystal. The peak at 644 nm is close to the predicted photonic band gap position for the probed direction (band diagram in Figure 3.13). Images of b) the depth and c) phase of the modulation (in degrees) of transmitted light with the rotation of crossed polarizers measured at a wavelength of 650nm, which is inside the band gap. The electric field direction relative to this image is vertical. The field of view in both (b) and (c) is $600 \mu\text{m}$ across.

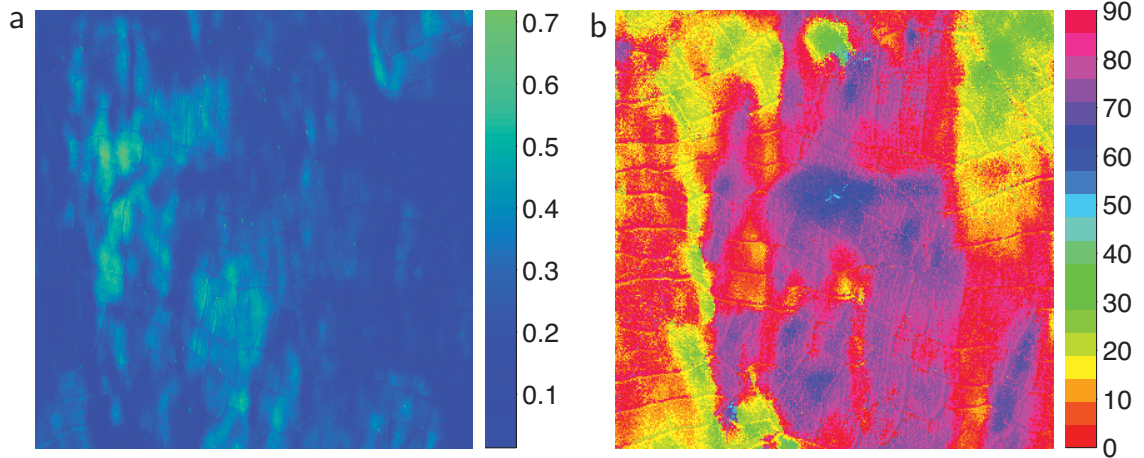


Figure 3.15: Images of a) the depth and b) phase of the modulation (in degrees) of transmitted light with the rotation of crossed polarizers measured at a wavelength of 534 nm, which is outside the band gap. The electric field direction relative to this image is vertical. The field of view in both (a) and (b) is $600 \mu\text{m}$ across.

underlying suspension structure.

Chapter 4

Conclusions and Future Work

Structural colors in nature and man-made photonic crystals have provided beautiful examples of the interaction between light and matter. In the cases of periodic structures, especially those composed of spheres, relatively straight forward calculations are sufficient to predict which colors of light will constructively interfere upon scattering. With the realization that non-periodic structures can also cause selective scattering and the development of synthesis techniques for producing large numbers of optical-scale non-spherical particles, I have tried to broaden our concept of structural colors and photonic crystals.

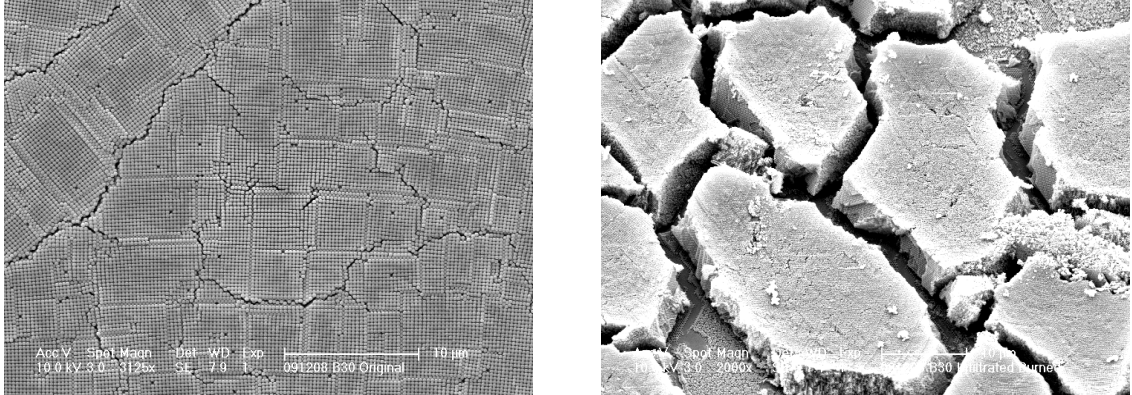
4.1 Isotropic Structural Color

Non-iridescent structural color is realized when an isotropic structure has a peak in $I(q)$ and wavelength-independent scattering is suppressed. We use a bidisperse mixture of spheres to frustrate crystallization and produce an isotropic structure. We find that controlling film thickness or absorption length are effective at enhancing contrast in reflectance spectra. These films may have applications in coatings, cosmetics and textiles. While the basic optical properties of structurally-colored feathers have

been reproduced, more work must be done before the biomimetic samples perform as well as their biological counterparts.

I believe that the most significant cause of the difference in performance between our biomimetic structures and those found in feathers is the inverse arrangement of high and low indices of refraction. Specifically, the scattering at short wavelengths produced by the colloid films is enhanced by the fact that the spheres have a higher index of refraction than their surroundings. The local index of refraction environment has been shown to have a significant impact on the scattering behavior of these types of materials [55]. The most obvious way to test this would be to invert the biomimetic structures to create an array of low index spheres in a high index background. There are methods that have been used to create inverse opals which involve the infiltration of an inorganic liquid precursor into a pre-formed colloidal crystal which undergoes a sol-gel reaction to fill the voids between particles with a material such as titania or silica [56]. The infiltration and deposition step is followed by heating the composite material to a temperature high enough to cause depolymerization and evaporation of the polymer template, leaving behind an inverted structure. Both of these steps generate significant stresses in the original structure and lead to shrinkage and cracking. Figure 4.1 shows the results of such a procedure, the small domains left behind after this procedure make it difficult to obtain high quality optical spectra. A technique that avoids the formation of cracks has been developed [1] and involves depositing the inorganic background material and the colloidal structure simultaneously. A demonstration of the results of this technique is shown in Figure 4.2. I have been able to produce centimeter-scale areas of crack free silica air-in-silica structures using this procedure. This technique should allow for the creation of inverted versions of the structures described in Chapter 2, provided that the co-deposition of the background material does not interfere with the formation

of the necessary isotropic structures.



(a) SEM image of a colloidal crystal before infiltration.

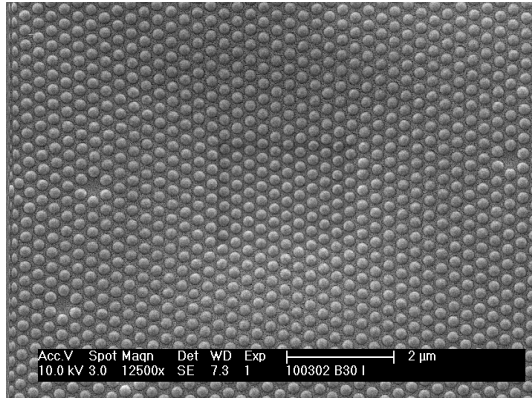
(b) SEM image of the silica structure after infiltration and burn-out following a procedure similar to that described in Ref. [56].

Figure 4.1: *Traditional inversion techniques cause cracking.*

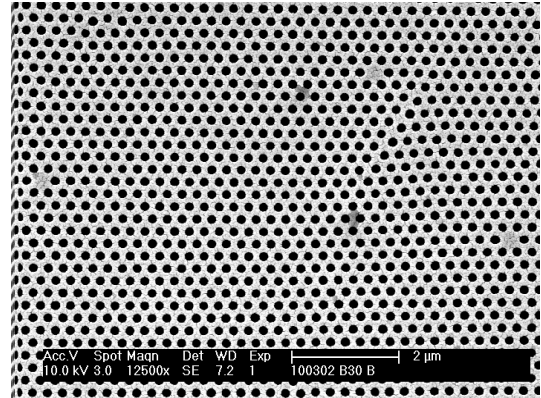
Another exciting possibility for an application of isotropic structural colors may result from the combination of this work with other research from our lab on the electrostatic interactions of colloids in non-polar solvents [57, 58, 59]. One conclusion drawn from studying the electrostatics of particles in non-polar solvents is that the interaction between a pair of particles is influenced by the presence of a third particle in a way that is not pair-wise additive [59]. We expect that the presence of an external field will also influence the interaction of particles in oil. The idea, then, is that the spacing between particles in a dense suspension can be tuned by applying an external electric field. With particle sizes and separations the right scale to scatter visible light, it may be possible to build a device displaying isotropic structural color that can be altered dynamically by varying an applied electric field.

4.2 Dumbbell Crystals

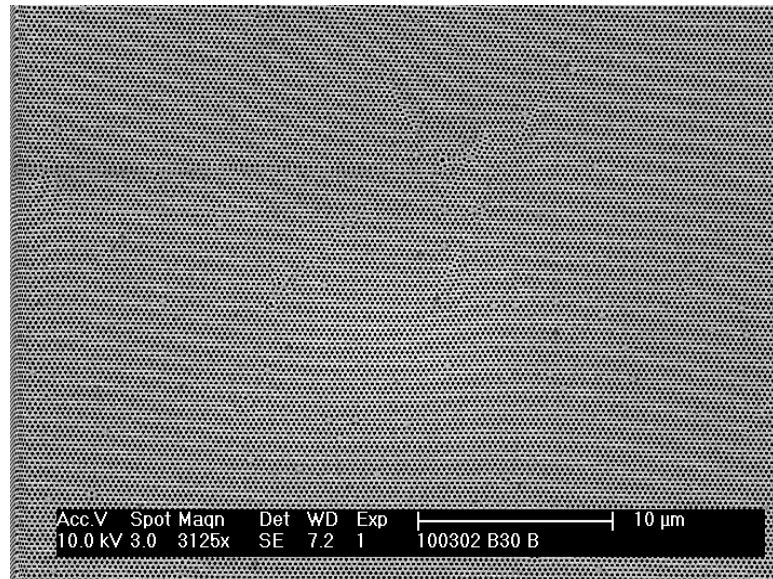
We describe the self assembly of non-spherical particles into crystals with novel structure and optical properties combining a partial photonic bandgap with birefringence



(a) SEM image of colloidal crystal prepared following the methods in Ref. [1].



(b) SEM image of the inverse structure achieved after burn-out following Ref. [1].



(c) Low-magnification SEM image of inverse structure.

Figure 4.2: *Simultaneous deposition of inorganic background and colloidal template prevents cracking.*

that can be modulated by an external field or quenched by solvent evaporation. Specifically, we study symmetric optical scale polymer dumbbells with an aspect ratio of 1.58. Hard particles with this geometry have been predicted to crystallize in equilibrium at high concentrations. However, experiments have shown that unlike spherical particles which readily crystallize in the bulk, these dumbbells crystallize only under strong confinement - in thin films less than three particles thick. Here, we demonstrate the use of an external electric field to align and assemble the dumbbells to make a birefringent suspension with structural color. When the electric field is turned off, the dumbbells rapidly lose their orientational order and the color and birefringence quickly go away. In this way, dumbbells combine the structural color of photonic crystals with the field addressability of liquid crystals. In addition, we find that if the solvent is removed in the presence of an electric field, the particles self assemble into a novel, dense crystalline packing hundreds of particles thick. Analysis of the crystal structure indicates that the dumbbells have a packing fraction of 0.7862, higher than the densest known packings of spheres and ellipsoids. We perform numerical experiments that demonstrate the importance of controlling the orientation of the dumbbells during drying for crystal formation.

The response of a suspension of dumbbells to an AC electric field described in Chapter 3 is quite striking. However, before this system can be developed into a useful optical device, it is necessary to have a clearer idea of the structures formed in suspension. Based on the optical properties of the suspension in a field, it seems reasonable that the structure is crystalline, but without a direct measurement we cannot be certain about the exact structure. The SAXS technique we use to study the structurally-colored materials in Chapter 2 could be used to study the structures formed by dumbbells in external fields. It would be interesting to explore the possibility of annealing the crystal structure formed in an electric field by cycling

the field on and off.. Finally, optimizing the speed with which the birefringence and structural color can be switched on and off by working with higher volume fractions, smaller chamber dimensions, or stronger fields would help in identifying potential applications for such a device.

4.3 Beyond Photonics

The size and shape of the dumbbells used in this dissertation have allowed us to assemble a new type of photonic crystal. The synthesis procedure described in Ref. [3] and in Appendix A gives us control over the surface chemistry, and hence the hydrophilic/hydrophobic character of each lobe. For example, the dumbbells used in Chapter 3 inherently possess an anisotropic surface chemistry. The surface of one of the lobes is the same as the polystyrene-co-trimethoxysilylpropylacrylate (poly(Styrene-co-TMSPA)) core-shell spheres described in A.2. The TMSPA comonomer introduces trimethoxysilane groups to the polymer which allows for the covalent attachment of a variety of other chemical species via silane chemistry [60]. The second lobe introduced in the final synthesis step is composed of only polystyrene sulfonate and is not susceptible to modification by silylation. Generally speaking, the difference in surface chemistry between the two lobes at this stage should give them some degree of amphiphilicity, but we can take advantage of the siloxane groups to increase the hydrophobicity of the poly(Styrene-co-TMSPA) lobe. One species we have done preliminary experiments with is N-[3-(Trimethoxysilyl)propyl]ethylenediamine (AEAPTS). A detailed analysis of the properties of these “amphiphilic” dumbbells has yet to be carried out so I will refrain from an in-depth description of them. I will, however, describe a few examples of the behavior of these dumbbells at an oil/water interface.

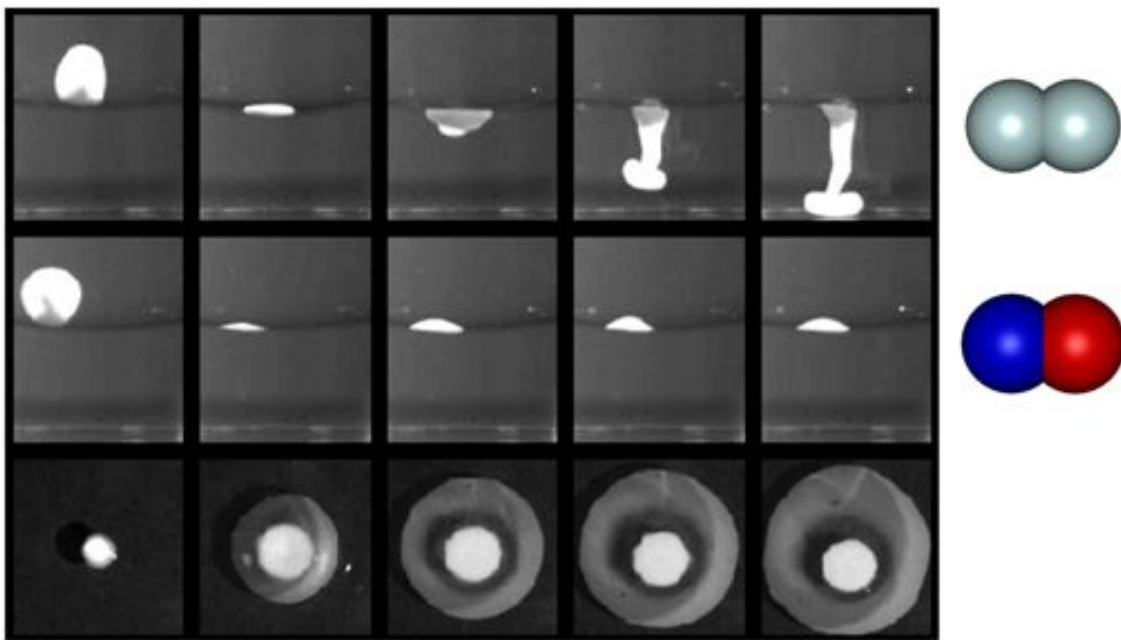


Figure 4.3: *Amphiphilic dumbbells spread at an oil/water interface* *Top Row:* Still frames from a side-view movie of an aqueous droplet of dumbbells with an isotropic surface chemistry impacting an oil/water interface. *Middle Row:* Still frames from a side-view movie of an aqueous droplet of dumbbells with an amphiphilic surface chemistry impacting an oil/water interface. *Bottom Row:* Still frames from a top-view movie of an aqueous droplet of dumbbells with an amphiphilic surface chemistry impacting an oil/water interface. Frames in each row are separated from each other by 42 ms. The first image in the bottom row is 11 s after the drop impacted the interface.

One demonstration of the affinity of amphiphilic dumbbells for oil/water interfaces is presented in Figure 4.3. When an aqueous droplet containing dumbbells with an isotropic surface chemistry (produced by introducing a mixture of styrene and TMSPA monomers in the final swelling step, see Appendix A.3) impacts the interface between oil (hexadecane) and water, the particles enter the water phase as a droplet and eventually spread by diffusion and convection. A droplet containing the amphiphilic dumbbells described above behaves very differently. Upon impact the droplet is trapped at the interface, usually for a few seconds but sometimes as long as five minutes. At some point the droplet suddenly breaks through the interface but the dumbbells do not enter the water phase. Instead, they rapidly spread across the oil/water interface and remain at the interface as long as we have observed the sample afterwards, up to about a week.



Figure 4.4: *Amphiphilic dumbbells impart elasticity to an oil/water interface.* Digital photographs of a membrane formed by amphiphilic dumbbells at a hexadecane/water interface being probed with a wooden stirrer.

We have also observed amphiphilic dumbbells impart elasticity upon oil/water interfaces. In Figure 4.4 we see that the membrane formed by amphiphilic dumbbells at the interface between hexadecane and water is elastic enough to prevent a wooden stirrer from breaking through the interface. As the stirrer is moved around, the dumbbell-covered interface deforms up to at least a centimeter while maintaining its integrity. This procedure is reversible, the stirrer can be removed and reinserted

many times without breaking through the interface.

The two demonstrations provided here suggest that amphiphilic dumbbells behave like colloidal surfactants and I expect that they will recapitulate many of the same phenomena. Particularly, it would be interesting to explore the ability for dumbbells to stabilize emulsions. Particle stabilized emulsions have been studied for more than a century ([61, 62]) and are often referred to as Pickering emulsions. So far, only spherical particles have been used to produce Pickering emulsions. I suspect that the non-spherical shapes of dumbbells will result in emulsions with unique properties. Specifically, exploring the role of the size ratio of the two lobes in stabilizing droplets of different sizes would be very exciting. Dumbbells with equally sized lobes should tend to stabilize larger droplets than dumbbells with one lobe significantly smaller than the other.

As we have seen, particles that are non-spherical can exhibit a variety of behaviors that spheres cannot. Dumbbells, however, are just one type of anisotropic particle. Another route to producing non-spherical particles that I have briefly explored is the compression of soft spheres to produce rhombic dodecahedra. Adding a small amount of toluene, which is a good solvent for polystyrene and immiscible with water, to an aqueous suspension of polystyrene spheres causes the spheres to swell and soften. Allowing the water to evaporate from this suspension generates a crystalline, usually face-centered cubic, packing of spheres which are eventually compressed by capillary forces as the final traces of water evaporate. SEM images, like the one in Figure 4.5, of the final structure shows that after drying the compressed particles retain their polygonal shape. The exact shape is presumed to be a rhombic dodecahedra since this is the space filling polygon that has the same unit cell as an FCC crystal of spheres. If these polygons can be resuspended, it would be very interesting to study their self-assembly behavior, especially to see whether they will assemble into the

densely-packed arrangement from which they were made or if they adopt some new structure accessible now due to their polygonal shape. The structures formed by colloidal polyhedra are just beginning to be explored [63].

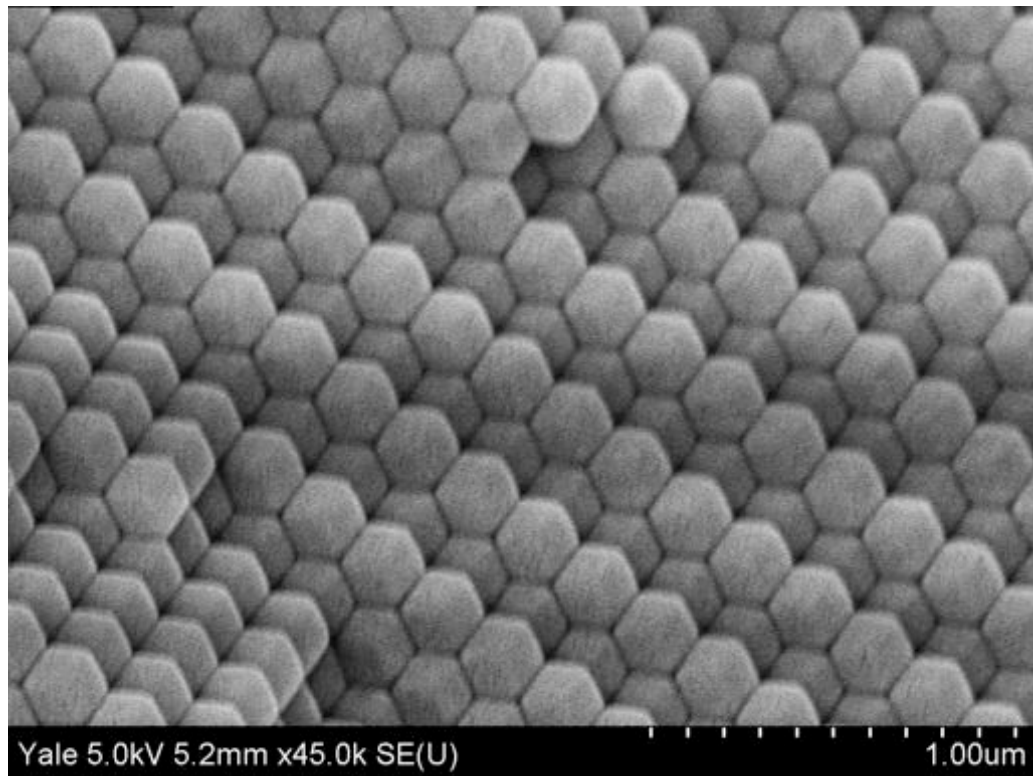


Figure 4.5: *Rhombic dodecahedra formed by capillary induced compression of toluene-swollen polystyrene spheres.*

Appendix A

Polymer Colloid Synthesis

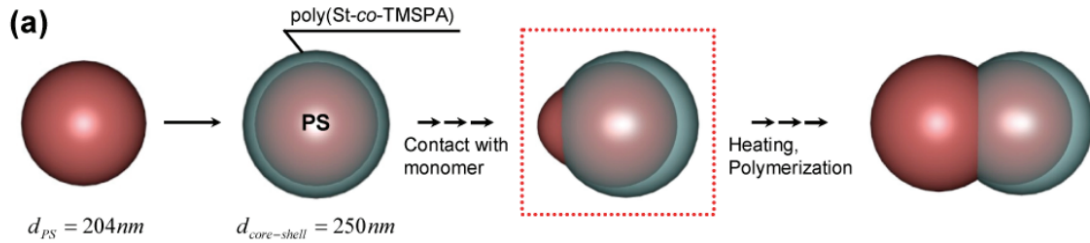


Figure A.1: *Schematic of the synthesis procedure used to make dumbbells.* From Ref. [3]

The synthesis procedure for all the particles used in this dissertation is illustrated in Figure A.1. The spherical polystyrene particles used in Chapter 2 correspond to the red sphere on the left of Figure A.1. The polystyrene spheres are then swollen with a mixture of styrene and TMSPA monomers. After polymerizing the new monomer, we have the spherical core-shell poly(sty-co-TMSPA) particles that are illustrated in the second step of Figure A.1. Adding and polymerizing new monomer a second time does not result in larger spheres, instead, the newly polymerized material forms a second lobe and we have the dumbbell particles used in Chapter 3 and illustrated in the final step of Figure A.1.

A.1 Polystyrene Sulfonate Spheres

The synthesis of polystyrene-sulfonate spheres begins with the assembly of a 500 mL three-neck round-bottom flask fitted with a cold-water reflux condenser, teflon blade stirrer, and a nitrogen inlet. The assembled reaction vessel is lowered into a temperature controlled water bath set to 65° C. While waiting for the bath to come up to temperature, the reagents are prepared. First, methanol and DI water in the quantities indicated in Figure A.2a are combined in a 250 mL glass bottle. Second, the indicated quantity of ionic co-monomer, 4-vinylbenzenesulfonate (VBS), is added to the methanol/DI solution and shaken to dissolve. Third, the appropriate amount of water-soluble initiator, potassium persulfate (KPS), is added to the methanol/DI/VBS solution and shaken to dissolve, which for KPS can take a few minutes. Fourth, the styrene monomer is pipetted from the stock bottle into a 40 mL glass vial. Once the water bath temperature reaches 65° C and the KPS has completely dissolved, the methanol/DI/VBS/KPS solution is poured into the reaction vessel, the stirring speed is set to 400 RPM, and the atmosphere in the vessel is purged with a quick burst of nitrogen. In practice, the stir speed should be as fast as possible without causing the liquid to splash into the connecting joints of the flask. Adding the room temperature solution to the reaction vessel will cause the temperature to drop. Once the water bath temperature has recovered, the styrene monomer is poured into the reaction vessel and the nitrogen is set to slowly flow through the vessel as the polymerization reaction proceeds for at least eight hours, although longer reaction times will result in more complete conversion of monomer into polymer.

Figure A.2b shows an SEM image of the spheres produced by using the quantities of reagents listed in Figure A.2a.

There are a multiple ways to change the final size of particles synthesized with this technique including changing the quantity of VBS, the quantity of styrene, or the quantity of methanol [32]. The different size spheres used in Chapter 2 are made by varying the amount of methanol in the reaction while keeping the combined volume of DI water and methanol constant. As described in Ref. [32], increasing the fraction of methanol results in larger diameter spheres if the quantities of all the other reagents are fixed.

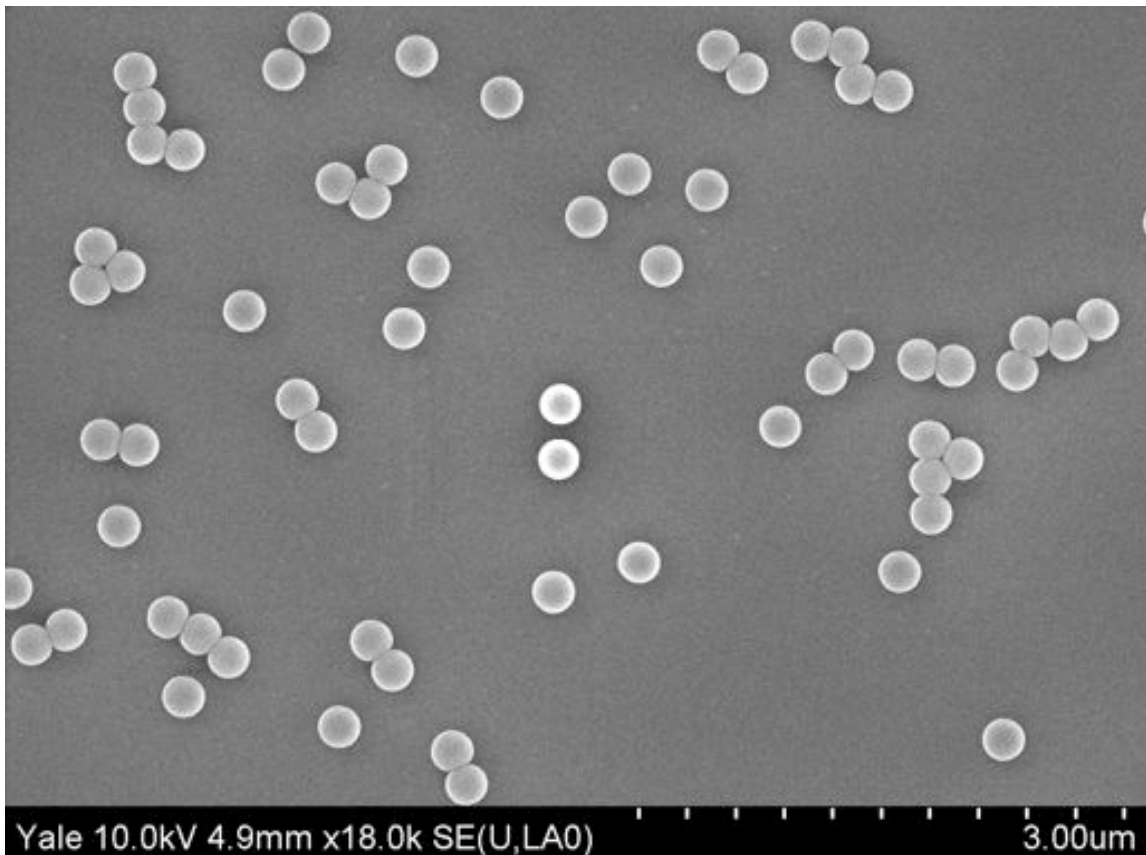
It should be noted that the final composition of spheres made with the formulation in Figure A.2a is not the only possible formulation. Methacrylic acid and divinylbenzene have both been successfully incorporated with styrene using this procedure. When methacrylic acid is included, typically in quantities up to 10% of the total monomer, the resulting polymer is a random co-polymer of styrene and methacrylic acid with carboxylic acid groups present on the surface of the spheres. These carboxylic acid groups can then be used to covalently attach other species. For example, proteins are frequently attached to particles presenting carboxylic acid via carbodiimide chemistry. When divinylbenzene is included in the monomer mixture, typically in quantities up to a few percent of the total monomer, the resulting polymer network is no longer composed of linear polymer chains but is composed of polymer chains which are covalently cross-linked. Cross-linking particles have a very different physical character than linear polymer particles and are desirable for many uses because of their limited ability to swell [64].

A.2 Poly(styrene-co-TMSPA) Core-Shell Spheres

Polystyrene spheres as synthesized by the procedure in the previous section are the starting material for the synthesis of core-shell poly(styrene-co-TMSPA) spheres.

111010		Batch 46		Notes
Step	Ingredient	Quantity	Units	
1-1	DI Water	167	mL	Mix 1-1 ingredients in a 250 mL glass bottle. Start heating water bath to 65C and assemble reaction vessel.
	Methanol	49	mL	
	4-vinylbenzenesulfonate	0.272	g	
1-2	Potassium persulfate	0.145	g	After 4-VBS has dissolved and water bath is at temperature, mix KPS with solution from 1-1. Once dissolved, charge the reaction vessel and stir at 400 RPM.
2	Styrene	34	mL	If using multiple monomers, mix together before charging the reaction vessel.
3				Allow reaction to proceed at least 8 hours. More time is ok, i.e. overnight.
Total volume	% Methanol	Theoretical Yield (vol. fraction)		Taking into account the density of styrene monomer (0.909) and density of polystyrene (1.06), assuming 100% conversion and no solvent loss.
250	19.6	0.119		

(a) Details of the synthesis of polystyrene sulphonate spheres.



(b) SEM image of the polystyrene spheres resulting from the recipe detailed in Figure A.2a.

Figure A.2: *Polystyrene sulfonate sphere synthesis.*

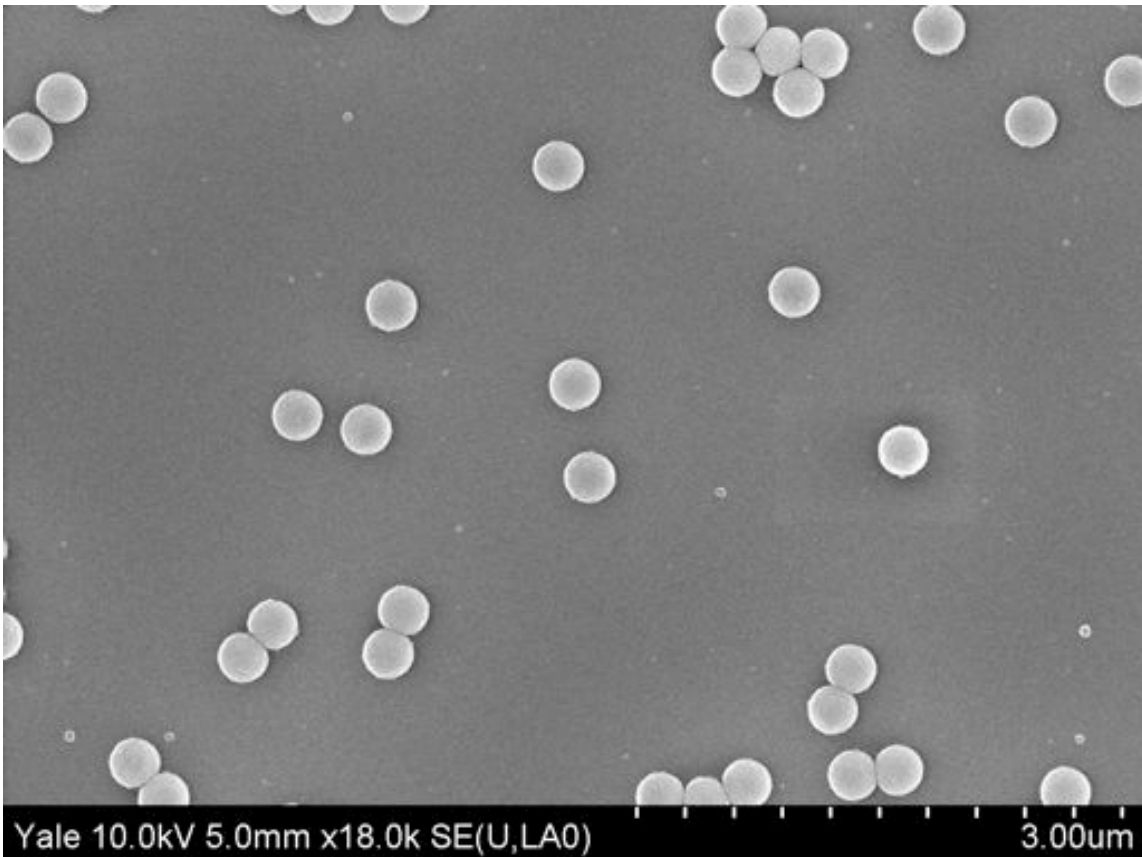
Figure A.3a contains the information for four identical batches of core-shell particles that are synthesized simultaneously in separate reaction vials. In general, though, each reaction vial can contain a different composition. The core-shell particles used to make the dumbbells used in Chapter 3 are prepared as follows, using the recipe shown in Figure A.3a. First, a temperature controlled water bath is set to 70° C. Second, 15 mL of as-synthesized polystyrene sulfonate spheres are combined with 12 mL of DI water in a 40 mL glass vial. Third, 9.9 mg of oil-soluble initiator, azobisisobutyronitrile (AIBN), is weighed into a 20 mL glass vial. Fourth, 1.78 mL of styrene monomer and 0.20 mL of TMSPA are added to the vial containing AIBN and shaken to dissolve. Once the AIBN has dissolved, 1.79 mL of the monomer mixture is added to the 40 mL vial containing the polystyrene sphere suspension. The 40 mL vial is then closed, sealed with teflon tape and mixed by vortexing for one minute. This procedure is repeated if more than one core-shell synthesis is being done simultaneously. The reaction vials are then loaded into a plastic bottle which has been fixed to a metal stirring shaft. The entire assembly is attached to a mixer and submerged in the 70° water bath while rotating at approximately 300 RPM. The polymerization reaction is allowed to proceed for at least eight hours, but longer reaction times will result in more complete conversion of monomer to polymer.

Figure A.3b shows an SEM image of the core-shell spheres produced by using the quantities of reagents listed in the first column of Figure A.3a.

The surface of the core-shell spheres is composed of a random co-polymer of styrene and TMSPA. As discussed in Chapter 4, the TMSPA is not only necessary for the production of dumbbells, it also allows for the covalent attachment of other chemical species via silane chemistry which can significantly alter the nature of the surface [60].

	Name Date	CS018 111020	CS019 111020	CS020 111020	CS021 111020		
Seed dispersion	PS sphere suspension	15.00 mL	B46	15.00 mL	B46	15.00 mL	B46
	Water	12.00 mL		12.00 mL		12.00 mL	12.00 mL
Monomers	1st monomer	1.61 mL	Styrene	1.61 mL	Styrene	1.61 mL	Styrene
	2nd monomer	0.18 mL	TMSPA (new)	0.18 mL	TMSPA (new)	0.18 mL	TMSPA (old)
	3rd monomer						TMSPA (new)
Initiator	Initiator	0.009 g	AIBN (new)	0.009 g	AIBN (new)	0.009 g	AIBN (new)
							AIBN (old)
Reaction Conditions	Temperature	70 C		70 C		70 C	
	Tumbling speed	300 RPM		300 RPM		300 RPM	
Factors determining recipe	Volume fraction of PS sphere suspension	0.119	B46	0.119	B46	0.119	B46
	Total monomer swelling Ratio (vol/vol)	1.00		1.00		1.00	
	Ratio of TMSPA to total new monomer (vol/vol)	0.10		0.10		0.10	
Calculations	Theoretical yield volume fraction	0.117		0.117		0.117	
Monomer solution recipe	Styrene	3.53 mL		styrene	1.76715	styrene	1.76715
	TMSPA (new)	0.39 mL		TMSPA (old)	0.19635	TMSPA (new)	0.19635
	AIBN (new)	0.020 g		AIBN (new)	0.0098175	AIBN (old)	0.0098175

(a) Details of the synthesis of poly(styrene-co-TMSPA) core-shell spheres.



(b) SEM image of the poly(styrene-co-TMSPA) core-shell spheres resulting from the recipe detailed in the first column of Figure A.3a (CS018).

Figure A.3: *Poly(Styrene-co-TMSPA) core-shell sphere synthesis.*

A.3 Dumbbells

Core-shell spheres as synthesized by the procedure in the previous section are the starting material for the synthesis of dumbbells. Figure A.4a contains the information for four batches of dumbbell particles that are synthesized simultaneously in separate reaction vials. In general, each reaction vial can contain a different composition. The dumbbells used in Chapter 3 are prepared as follows, using the recipe shown in Figure A.4a. First, a temperature controlled water bath is set to 70° C. Second, 7 mg of VBS is dissolved in 8 mL of DI water and added to the core-shell suspension. Third, 8 mL of as-synthesized poly(styrene-co-TMSPA) spheres are combined with 3.5 mL of DI water and 1 mL of 1% (w/w) Pluronic F108 in DI water in a 40 mL glass vial. Fourth, 5.5 mg of oil-soluble initiator, azobisisobutyronitrile (AIBN), is weighed into a 20 mL glass vial. Fifth, 1.03 mL of styrene monomer is added to the vial containing AIBN and shaken to dissolve. Once the AIBN has dissolved, 0.94 mL of the monomer mixture is added to the 40 mL vial containing the core-shell sphere suspension. The 40 mL vial is then closed, sealed with teflon tape and mixed by vortexing for one minute. This procedure is repeated if more than one dumbbell synthesis is being done simultaneously. The reaction vials are then loaded into a plastic bottle which has been fixed to a metal stirring shaft. The entire assembly is attached to a mixer and submerged in the 70° water bath while rotating at approximately 300 RPM. The polymerization reaction is allowed to proceed for at least eight hours, but longer reaction times will result in more complete conversion of monomer to polymer.

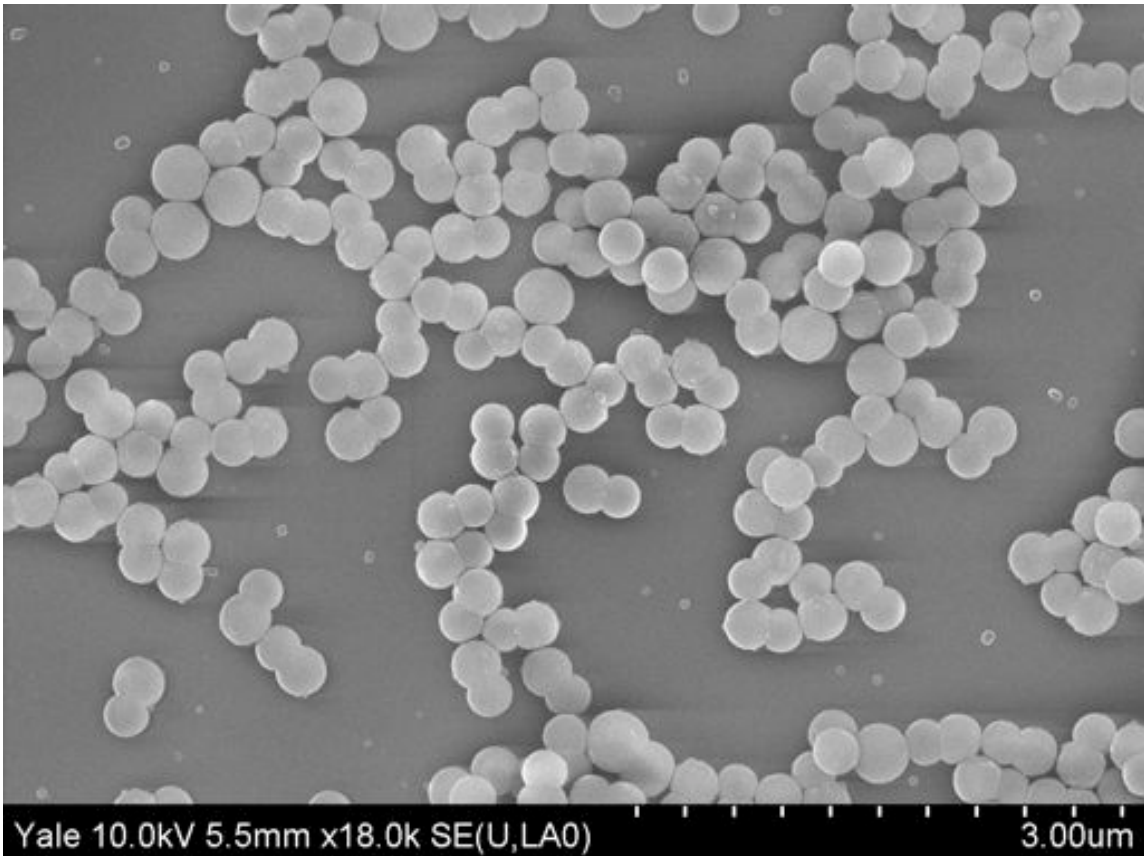
Figure A.4b shows an SEM image of the dumbbells produced by using the quantities of reagents listed in the first column of Figure A.4a. Figure A.5 shows a high-magnification SEM image of the same dumbbells shown in Figure A.4b and

highlights the difference in roughness between the poly(Styrene-co-TMSPA) lobe and the newly-formed polystyrene lobe.

This procedure for making dumbbells can be modified to produce particles with varying aspect ratios and surface chemistries. The simplest way to vary the aspect ratio of a batch of dumbbells is to change the quantity of new monomer added. In the recipe highlighted here, the volume of new monomer is such that the new lobe of each dumbbell will be the same size as the core-shell seed particle. Adding more or less monomer will result in a larger or smaller new lobe, as demonstrated in Ref. [3]. The surface chemistry of the new lobe depends on the composition of added monomer and we have successfully synthesized dumbbells with isotropic surface chemistry by including TMSPA to the monomer mixture in this step. These isotropic dumbbells were used in the demonstration of dumbbell behavior at an oil/water interface in Chapter 4. Other monomers, such as methacrylic acid, can be included in the monomer mixture to provide enhanced chemical functionality.

Name Date		iDB09 111021		iDB10 111021		iDB11 111021		iDB12 111021	
Seed dispersion	Core-shell suspension	8.00 mL	CS018	8.00 mL	CS019	8.00 mL	CS020	8.00 mL	CS021
	Water	3.50 mL		3.50 mL		3.50 mL		3.50 mL	
Ionic Co-polymer solution	1% F108	1.00 mL		1.00 mL		1.00 mL		1.00 mL	
	4-vinylbenzenesulfonate	0.007 g		0.007 g		0.007 g		0.007 g	
Monomers	water	8.00 mL		8.00 mL		8.00 mL		8.00 mL	
	1st monomer	0.94 mL	Styrene	0.94 mL	Styrene	0.94 mL	Styrene	0.94 mL	Styrene
	2nd monomer	0.00 mL	TMSPA	0.00 mL	TMSPA	0.00 mL	TMSPA	0.00 mL	TMSPA
Initiator	3rd monomer								
	Initiator	0.005 g	AIBN (new)	0.005 g	AIBN (new)	0.005 g	AIBN (new)	0.005 g	AIBN (new)
Reaction Conditions		Temperature 300 RPM	70 C	70 C 300 RPM		70 C 300 RPM		70 C 300 RPM	
Factors determining recipe	Volume fraction of core-shell suspension	0.117	CS018	0.117	CS019	0.117	CS020	0.117	CS021
	Total monomer swelling Ratio (vol/vol)	1.00		1.00		1.00		1.00	
	Ratio of TMSPA to total new monomer (vol/vol)	0.00		0.00		0.00		0.00	
Calculations		Theoretical yield volume fraction	0.131		0.131		0.131		0.131
Ionic Co-polymer solution recipe	Water	35.20 mL							
	4-vinylbenzenesulfonate	0.033 g							
Monomer solution recipe	Styrene	4.12 mL							
	TMSPA	0.00 mL							
	AIBN	0.021 g							

(a) Details of the synthesis of dumbbells.



(b) SEM image of the dumbbells resulting from the recipe detailed in the first column of Figure A.4a (jDB09).

Figure A.4: *Dumbbell synthesis*.

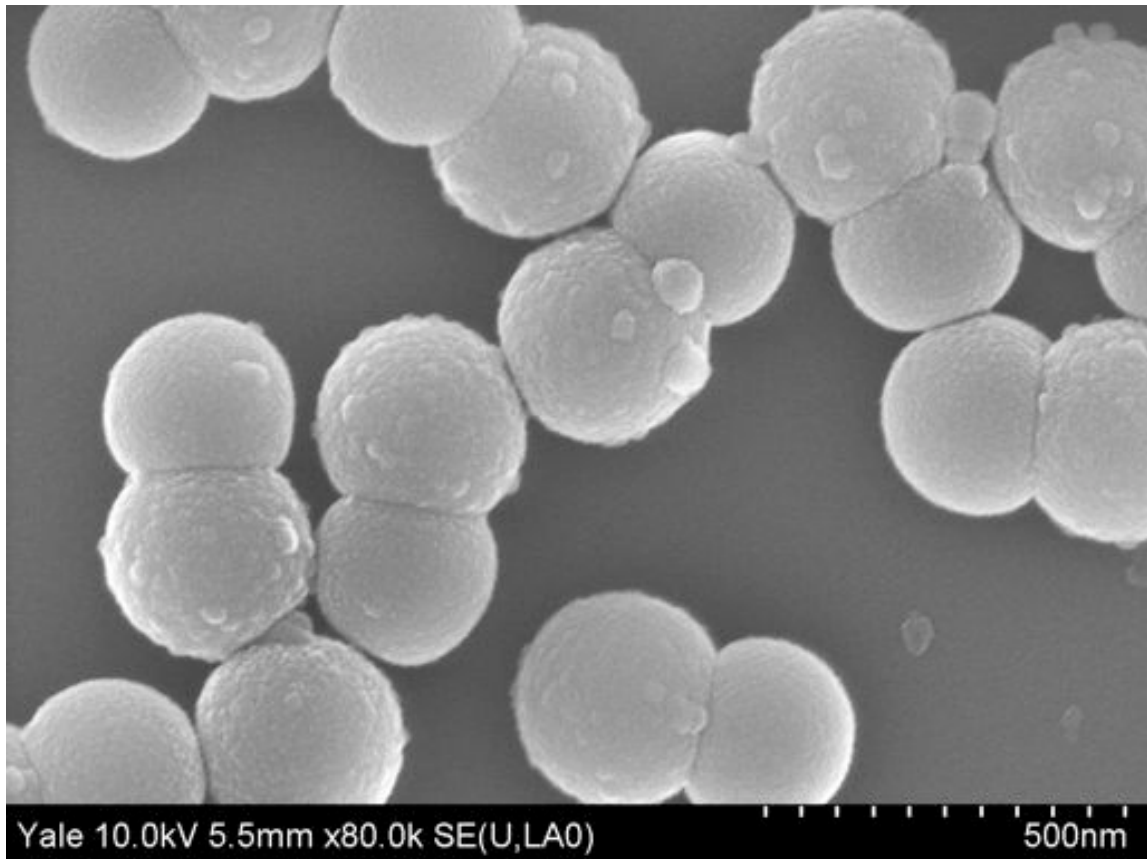


Figure A.5: *High-magnification SEM image of dumbbells.* High-magnification SEM image of the same dumbbells in Figure A.4b. Note that the two lobes have differing degrees of roughness. The smoother lobe is primarily polystyrene and the rougher lobe is poly(styrene-co-TMSPA).

Bibliography

- [1] Benjamin Hatton, Lidiya Mishchenko, Stan Davis, Kenneth H. Sandhage, and Joanna Aizenberg. Assembly of large-area, highly ordered, crack-free inverse opal films. *Proceedings of the National Academy of Sciences*, 2010.
- [2] Eric R. Dufresne, Heeso Noh, Vinodkumar Saranathan, Simon G. J. Mochrie, Hui Cao, and Richard O. Prum. Self-assembly of amorphous biophotonic nanostructures by phase separation. *Soft Matter*, 5(9):1792–1795, 2009.
- [3] Jin-Gyu Park, Jason D. Forster, and Eric R. Dufresne. High-yield synthesis of monodisperse dumbbell-shaped polymer nanoparticles. *Journal of the American Chemical Society*, 132:5960–5961, 2010.
- [4] Jason D. Forster, Jin-Gyu Park, Manish Mittal, Heeso Noh, Carl F. Schreck, Corey S. O’Hern, Hui Cao, Eric M. Furst, and Eric R. Dufresne. Assembly of optical-scale dumbbells into dense photonic crystals. *ACS Nano*, 5(8):6695–6700, 2011.
- [5] Mohan Srinivasarao. Nano-optics in the biological world: beetles, butterflies, birds, and moths. *Chemical reviews*, 99(7):1935–1961, 1999.
- [6] Peter Vukusic and J. Roy Sambles. Photonic structures in biology. *Nature*, 424, 2003.

- [7] Andrew R. Parker and Helen E. Townley. Biomimetics of photonic nanostructures. *Nature Nanotechnology*, 2:347–353, 2007.
- [8] V. L. Welch and J. P. Vigneron. Beyond butterflies—the diversity of biological photonic crystals. *Optical and Quantum Electronics*, 39:295–303, 2007.
- [9] S. Kinoshita, S. Yoshioka, and J. Miyazaki. Physics of structural colors. *Reports on Progress in Physics*, 71(7):076401 (30pp), 2008.
- [10] J. V. Sanders. Diffraction of light by opals. *Acta Crystallographica Section A*, 24(4):427–434, 1968.
- [11] Max Born and Emil Wolf. *Principles of Optics*. Cambridge University Press, seventh (expanded) edition, 1999.
- [12] Richard O. Prum, Rodolfo H. Torres, Scott Williamson, and Jan Dyck. Coherent light scattering by blue feather barbs. *Nature*, 396:28–29, 1998.
- [13] Vinodkumar Saranathan. *Evolutionary photonics: structure, function, development and evolution of organismal structural color*. PhD thesis, Yale University, 2011.
- [14] Richard O. Prum, Eric R. Dufresne, Tim Quinn, and Karla Waters. Development of colour-producing beta-keratin nanostructures in avian feather barbs. *Journal of The Royal Society Interface*, 6:S253–S265, 2009.
- [15] Heeso Noh, Seng Fatt Liew, Vinodkumar Saranathan, Simon G. J. Mochrie, Richard O. Prum, Eric R. Dufresne, and Hui Cao. How noniridescent colors are generated by quasi-ordered structures of bird feathers. *Advanced Materials*, 22(26-27):2871–2880, 2010.

- [16] Adeline Perro, Stephane Reculusa, Serge Ravaine, Elodie Bourgeat-Lami, and Etienne Duguet. Design and synthesis of Janus micro- and nanoparticles. *Journal of Materials Chemistry*, 15:3745–3760, 2005.
- [17] Shan Jiang, Mitchell J. Schultz, Qian Chen, Jeffrey S. Moore, and Steve Granick. Solvent-free synthesis of Janus colloidal particles. *Langmuir*, 24:10073–10077, 2008.
- [18] Etienne Duguet, Anthony Desert, Adeline Perro, and Serge Ravaine. Design and elaboration of colloidal molecules: an overview. *Chemical Society Reviews*, 40:941–960, 2011.
- [19] Anke Kuijk, Alfons van Blaaderen, and Arnout Imhof. Synthesis of monodisperse, rodlike silica colloids with tunable aspect ratio. *Journal of the American Chemical Society*, 133:2346–2349, 2011.
- [20] Eli Yablonovitch. Inhibited spontaneous emission in solid-state physics and electronics. *Physical Review Letters*, 58(20):2059–2062, 1987.
- [21] Sajeev John. Strong localization of photons in certain disordered dielectric superlattices. *Phys. Rev. Lett.*, 58:2486–2489, Jun 1987.
- [22] G. G. Stokes. On a remarkable phenomenon of crystalline reflection. *Proceedings of the Royal Society of London*, 38:pp. 174–185, 1884.
- [23] John D. Joannopoulos, Steven G. Johnson, Joshua N. Winn, and Robert D. Meade. *Photonic Crystals: Molding the Flow of Light*. Princeton University Press, 2008.
- [24] Vitalij Pecharsky and Peter Zavalij. *Fundamentals of Powder Diffraction and Structural Characterization of Materials*. Kluwer Academic Publishers, 2003.

- [25] Heeso Noh, Seng Fatt Liew, Vinodkumar Saranathan, Richard O. Prum, Simon G. J. Mochrie, Eric R. Dufresne, and Hui Cao. Contribution of double scattering to structural coloration in quasiordered nanostructures of bird feathers. *Physical Review E*, 81:051923, May 2010.
- [26] Andrew R. Parker. A vision for natural photonics. *Philosophical Transactions of the Royal Society A: Mathematical, Physical and Engineering Sciences*, 362(1825):2709–2720, 2004.
- [27] Susumu Noda and Toshihiko Baba. *Roadmap on Photonic Crystals*. Kluwer Academic Publishers, 2003.
- [28] C. M. Soukoulis. *Photonic Crystals and Light Localization in the 21st Century*. Springer, 2001.
- [29] M. Muller, R. Zentel, T. Maka, S. G. Romanov, and C. M. Sotomayor Torres. Photonic crystal films with high refractive index contrast. *Advanced Materials*, 12(20), 2000.
- [30] Benny T. Hallam, Anthony G. Hiorns, and Peter Vukusic. Developing optical efficiency through optimized coating structure: biomimetic inspiration from white beetles. *Applied Optics*, 48(17):3243–3249, 2009.
- [31] Yukikazu Takeoka, Masaki Honda, Takahiro Seki, Masahiko Ishii, and Hiroshi Nakamura. Structural colored liquid membrane without angle dependence. *ACS Applied Materials & Interfaces*, 1(5):982–986, 2009.
- [32] Y. Chonde and I. M. Krieger. Emulsion polymerization of styrene with ionic comonomer in the presence of methanol. *Journal of Applied Polymer Science*, 26(6):1819–1827, 1981.

- [33] Peng Jiang and Michael J. McFarland. Large-scale fabrication of wafer-size colloidal crystals, macroporous polymers and nanocomposites by spin-coating. *Journal of the American Chemical Society*, 126:13778–13786, 2004.
- [34] Guo-Jie Gao, Jerzy Bławdziewicz, and Corey S. O’Hern. Frequency distribution of mechanically stable disk packings. *Physical Review E*, 74(6):061304, Dec 2006.
- [35] Sharon C. Glotzer and Michael J. Solomon. Anisotropy of building blocks and their assembly into complex structures. *Nature Materials*, 6:380–382, 2007.
- [36] Yu Lu, Yadong Yin, and Younan Xia. Three-dimensional photonic crystals with non-spherical colloids and building blocks. *Advanced Materials*, 13(6):415–420, 2001.
- [37] Yu Lu, Yadong Yin, Zhi-Yuan Li, and Younan Xia. Colloidal crystals made of polystyrene spheroids: Fabrication and structural/optical characterization. *Langmuir*, 18:7722–7727, 2002.
- [38] Ian D. Hosein, Stephanie H. Lee, and Chekesha M. Liddell. Dimer-based three-dimensional photonic crystals. *Advanced Functional Materials*, 20:3085–3091, 2010.
- [39] H. R. Sheu, M. S. El-Aasser, and J. W. Vanderhoff. Phase separation in polystyrene latex interpenetrating polymer networks. *Journal of Polymer Science Part A: Polymer Chemistry*, 28(3):629–651, 1990.
- [40] C. Vega, E. P. A. Paras, and P. A. Monson. Solid-fluid equilibria for hard dumbbells via Monte Carlo simulation. *Journal of Chemical Physics*, 96(12):9060–9072, 1992.

- [41] Manish Mittal and Eric M. Furst. Electric field-directed convective assembly of ellipsoidal colloidal particles to create optically and mechanically anisotropic thin films. *Advanced Functional Materials*, 19:3271–3278, 2009.
- [42] Mark Grzelczak, Jan Vermant, Eric M. Furst, and Luis M. Liz-Marzan. Directed self-assembly of nanoparticles. *ACS Nano*, 4(7):3591–3605, 2010.
- [43] Ahmet F. Demirors, Patrick M. Johnson, Carlos M. van Kats, Alfons van Blaaderen, and Arnout Imhof. Directed self-assembly of colloidal dumbbells with an electric field. *Langmuir*, 26(18):14466–14471, 2010.
- [44] Seth Fraden, Alan J. Hurd, and Robert B. Meyer. Electric-field-induced association of colloidal particles. *Physical Review Letters*, 63(21):2373–2376, 1989.
- [45] Anand Yethiraj and Alfons van Blaaderen. A colloidal model system with an interaction tunable from hard sphere to soft and dipolar. *Nature*, 421:513–517, 2003.
- [46] Tieying Gong, David T. Wu, and David W. M. Marr. Electric-field reversible three-dimensional colloidal crystals. *Langmuir*, 19:5967–5970, 2003.
- [47] Manish Mittal, Pushkar P. Lele, Eric W. Kaler, and Eric M. Furst. Polarization and interactions of colloidal particles in ac electric fields. *Journal of Chemical Physics*, 129:064513, 2008.
- [48] Simon O. Lumsdon, Eric W. Kaler, Jacob P. Williams, and Orlin D. Velev. Dielectrophoretic assembly of oriented and switchable two-dimensional photonic crystals. *Applied Physics Letters*, 82(6):949–951, 2003.

- [49] Tao Ding, Kai Song, Koen Clays, and Chen-Ho Tung. Fabrication of 3D photonic crystals of ellipsoids: Convective self-assembly in magnetic field. *Advanced Materials*, 21:1936–1940, 2009.
- [50] Aleksandar Donev, Frank H. Stillinger, P. M. Chaikin, and Salvatore Torquato. Unusually dense crystal packings of ellipsoids. *Physical Review Letters*, 92(25):255506, 2004.
- [51] Guo-Jie Gao, Jerzy Blawdziewicz, and Corey S. O’Hern. Frequency distribution of mechanically stable disk packings. *Physical Review E*, 74(6):061304, 2006.
- [52] C. Vega, E. P. A. Paras, and P. A. Monson. On the stability of the plastic crystal phase of hard dumbbell solids. *Journal of Chemical Physics*, 97:8543–8548, 1992.
- [53] Aleksandar Donev, Ibrahim Cisse, David Sachs, Evan A. Variano, Frank H. Stillinger, Robert Connelly, Salvatore Torquato, and P. M. Chaikin. Improving the density of jammed disordered packings using ellipsoids. *Science*, 303:990–993, 2004.
- [54] Yiannis Monovoukas, Gerald G. Fuller, and Alice P. Gast. Optical anisotropy in colloidal crystals. *Journal of Chemical Physics*, 93:8294–8299, 1990.
- [55] Seng Fatt Liew, Jason D. Forster, Heeso Noh, Carl F. Schreck, Vinodkumar Saranathan, X. Lu, Lin Yang, Richard O. Prum, Corey S. O’Hern, Eric R. Dufresne, and Hui Cao. Short-range order and near-field effects on optical scattering and structural coloration. *Optics Express*, 19(9), 2011.
- [56] Rick C. Schroden, Mohammed Al-Daous, Christopher F. Blanford, and Andreas Stein. Optical properties of inverse opal photonic crystals. *Chemistry of Materials*, 14(8):3305–3315, 2002.

- [57] Sunil K. Sainis, Vincent Germain, Cecile O. Mejean, and Eric R. Dufresne. Electrostatic interactions of colloidal particles in nonpolar solvents: Role of surface chemistry and charge control agents. *Langmuir*, 24(4):1160–1164, 2008. PMID: 18062711.
- [58] Sunil K. Sainis, Jason W. Merrill, and Eric R. Dufresne. Electrostatic interactions of colloidal particles at vanishing ionic strength. *Langmuir*, 24(23):13334–13337, 2008.
- [59] Jason W. Merrill, Sunil K. Sainis, and Eric R. Dufresne. Many-body electrostatic forces between colloidal particles at vanishing ionic strength. *Physical Review Letters*, 103:138301, Sep 2009.
- [60] P. Van Der Voort and E. F. Vansant. Silylation of the silica surface a review. *Journal of Liquid Chromatography & Related Technologies*, 19(17-18):2723–2752, 1996.
- [61] W. Ramsden. Separation of solids in the surface-layers of solutions and 'suspensions' (observations on surface-membranes, bubbles, emulsions, and mechanical coagulation). – preliminary account. *Proceedings of the Royal Society of London*, 72(477-486):156–164, 1903.
- [62] S.U. Pickering. Cxcvi. - emulsions. *Journal of the Chemical Society, Transactions*, 91:2001–2021, 1907.
- [63] Joel Henzie, Michael Grünwald, Asaph Widmer-Cooper, Phillip L. Geissler, and Peidong Yang. Self-assembly of uniform polyhedral silver nanocrystals into densest packings and exotic superlattices. *Nature Materials*, advance online publication:–, 11 2011.

- [64] H. R. Sheu, M. S. El-Aasser, and J. W. Vanderhoff. Phase separation in polystyrene latex interpenetrating polymer networks. *Journal of Polymer Science Part A: Polymer Chemistry*, 28(3):629–651, 1990.